UNIVERSITY OF CALGARY

Experiments Towards the Realization of a Nanofiber Guided Dipole Trap

by

Di Chang

A THESIS

SUBMITTED TO THE FACULTY OF GRADUATE STUDIES

IN PARTIAL FULFILLMENT OF THE REQUIREMENTS FOR THE

DEGREE OF MASTER OF SCIENCE

GRADUATE PROGRAM IN PHYSICS AND ASTRONOMY

CALGARY, ALBERTA

December, 2015

Abstract

In this thesis I present a developing project to elaborate a scientific platform towards the realization of light-matter interaction based on tapered optical nanofiber (TNF) that enables optical fields to interface with trapped neutral atoms in their vicinity. In such a configuration, the guided light exhibits a large portion of evanescent field into the vacuum thus laser cooled atoms can couple to the fiber mode. By trapping and cooling atoms around the nanofiber I investigated the interaction of the atoms with the field.

My work presented in this thesis includes: Calculating the evanescent modes propagating through our fiber; Implementing fiber pulling setup using oxyhydrogen flame and analyzing nanofiber's thermal dynamics and degradation; Constructing a Rubidium 87 MOT and characterizing its critical parameters; Realizing some atom-light interface through an experiment on coupling spontaneously emitted photons from MOT into TNF; Calculating two-color dipole trap parameters for our nanofiber.

Acknowledgements

I would like to start by thanking my family. Even though my parents are far away in China, they allowed me the freedom of traveling so far away to explore the wild world and pursue whatever interests I had. They were only concerned with my happiness and encouraged me to search for a major that really stimulated my curiosity. My mom has always been very supportive to me for whatever decisions I made to my own life and study, which gave me enough confidence to go so far away.

Being given the opportunity to work on experimental physics has provided me the chance to work with wonderful people. First, I would like to acknowledge my supervisor, Alex Lvovsky, for his guidance and help as well as for allowing me to work in his lab for almost three years. I still remember the excitement from my heart as getting his acceptance into this group when I was still working on oil and gas exploration at University of Houston. Without him, I might never have a chance to explore something totally new and challenging. In the past three years, I learned a lot on physics, hands-on experience of optics/electronics as well as trouble-shooting technical skills. These experiences really stimulate my interests in being a hands-on scientist and even though I decided to graduate as a Master of Science student and join the industry, I believe that I will keep pursuing my true interests for the future career.

Very grateful to Professor Paul Barclay for sharing his fiber-pulling facilities and also for giving me advice on how to improve their performances. Sincere gratitude to Dr. Kartikeya Murari for his help in understanding electronic problems. Many thanks to Harishankar J and J. P. Hadden for their help when I was working in their lab.

I always feel so lucky to work with so many amazing colleagues: Aveek Chandra, first, we constructed the whole setup from scratch together and fought with so many detailed problems all the way through. I express my sincere gratitude to Dr. Arturo Lezama for getting us together and helping us to start on this project. Eugene Moiseev, the second main colleague I was working with,

shared a lot of deep understanding on the experiments. Much appreciation to Andrew M and Connor K, who were often bugged by my optical/electronic questions since I joined this group. I had lots of pleasure of working with people in the workshops: Andy R and Darren G in the scientific workshop, Edward C in the electronic workshop and Mark in the glass workshop. Through interesting cross-functional and thoughtful communication with them, I always got precious technical help and insightful advice.

I will never forget those long hours of pulling fibers, extracting and transferring fibers, feeding through fibers to midnight or even later with Aveek and my current partner, Paul Anderson. People working on everything in a clean room even feel so difficult of carrying a small piece of glass across a few feet, I believe that very few people quite understand the challenges we were facing and going through each time. I appreciate the positive attitude and persistence from my coworkers which kept me smiling until this moment. I can say with confidence that I am leaving this project in better hands.

Last but not least, without my mother-like Fae E and her family here, I would not have such a peaceful working and living environment to focus and finish my study. Only with all these love and care, I have got the courage for living, working and enjoying Calgary in her rugged mountains and white snowfields. I would like to thank my other colleagues as well: Zhongzhong Q, Travis B, Dongsheng W, Arina T, Fan Y and Shreyas J, who have helped and cared about me in many different ways. Things would not be the same without all these friendly, smart and nice people.

Table of Contents

List of Tables

List of Figures and Illustrations

List of Symbols, Abbreviations and Nomenclature

Symbol	Definition
AOM	Acousto-optic modulator
APD	Avalanche photodiode
ECDL	External cavity diode laser
HWP	Half wave plate
IPA	Isopropyl alcohol
LO	Local oscillator
MOT	Magneto-optical trap
N.A.	Numerical aperture
O.D.	Optical depth
PBS	Polarizing beam splitter
PD	Photodetector
PMF	Polarization maintained fiber
QWP	Quarter wave plate
^{87}Rb	Rubidium 87
RF	Radio frequency
SMF	Single mode fiber
SPCM	Single photon counting module
TA	Tapered amplifier
TNF	Tapered nanofiber
UHV	Ultra-high vacuum
VCO	Voltage-controlled oscillator
XPM	Cross phase modulation

Chapter 1

Introduction

The interaction between light and matter, at a fundamental level, where a single photon interacts with a single atom, has been extensively researched over the last two decades. The motivation behind this is the development of miniaturized and integrated technologies to build up hybrid quantum systems that allow quantum network, quantum computation and so on. Realization of light-atom interaction would benefit the development of quantum repeaters, quantum memories and so on thus a lot of effort has been put into enhancing this interface. The resonant scattering cross section of a single atom is on the order of the wavelength's square. For example, for Rb^{87} atoms, between transition from $F = 2$ in $5^2S_{1/2}$ to $F = 3$ in $5^2P_{3/2}$, we have $\sigma_{0(m_F=\pm2\rightarrow m_{F'}=\pm3)} \approx 3 \times 10^{-9}\text{cm}^2$[14], which is roughly the square of 550nm. Thus such interaction is in general very weak since it is almost impossible to focus the optical beam into an area $\sim \lambda^2$ without fast divergence. Thus in this case, the required level of nonlinearity, i.e., the ratio between σ_0 and the beam mode area A approaching 1, will not be satisfied. One popular choice to enhance it is to use a cavity to allow one photon passing through the position of the atom many times so that the same optical state can interact with the atom multiple times. This is to increase the effective atomic cross section. Also other types of resonant structures like microspheres, microtoroids or dielectric materials have also been developed for this purpose.

Apart from the interest on the above applications, there is also an interest in quantum-optical science to realize nonlinear interaction at single photon energy level. This will lead to unconditional universal quantum computation with photons as well as methods for preparing and measuring photon number states. For example, cross-phase modulation (XPM) based on electromagnetically induced transparency (EIT), proposed by Schmidt and Imamoglu [1], has shown that a large XPM can be created without the hindrance of absorption but is limited by the effect of pulse

bandwidth.

To enhance this nonlinear interaction, we can try either to enhance the nonlinear property of the medium or to increase the intensity of the light field. An example for the former choice is to pursue a large optical depth $O.D. = \eta\sigma_0 L$ of the medium itself, in which η is the medium density and L is the interaction length. In the MOT system, η has an upper limit due to atomic collisions so the only freedom is to increase the interaction length as much as possible. And for the latter choice, the light field needs also to be focused as much as possible, $\sim \lambda^2$, without too much divergence. Optical nanofiber is a good candidate to meet both of these two criteria through offering a long interaction length with a high field intensity.

A tapered nanofiber (TNF) is fabricated by heating and stretching a commercial optical fiber, bringing its diameter from a few tens of μm to a few hundreds of nm. Such a fiber offers a strong transverse confinement of the guided mode while exhibiting a pronounced evanescent field surrounding its tapered region. As a comparison, a laser beam of wavelength 780nm focused to its own wavelength scale, has a Rayleigh length of $z_R = \frac{\pi w_0^2}{\lambda} \approx 2.45\mu$m, which is fairly short for interacting with cold Rubidium (Rb) atoms. In contrast, the TNF can guide the evanescent field over the whole taper length, typically several mm while the beam mode area guided through the TNF is proportional to and constantly consistent with the square of the wave-field decay length (the same order as the wavelength). This allows a high intensity at a low input power, which makes TNF an ideal tool to study nonlinear quantum optics.

In this thesis, I will present my work on building such a MOT-TNF interface platform. Chapter 2 gives the theoretical discussion on wave propagation in step-index optical fibers and TNF, our fabrication of TNF as well as an experiment we did to analyze the TNF's thermal dynamics. Chapter 3 talks about the principle of magneto-optical trap (MOT), its characterization and some experiments we did by overlapping the TNF and MOT. Finally, I conclude my thesis and give some outlook in Chapter 4.

Chapter 2

Light propagation in optical fibers

In this chapter, light propagation in optical fiber and tapered nanofiber will be discussed in section 1 and 2, respectively. Fields calculation for our tapered nanofiber (TNF) is given in section 3 and fabrication details will be described in section 4.

2.1 Solution for the fields in step-index optical fibers

Here, we only analyze optical fibers with structure of circular step-index. Light rays incident into the core-cladding boundary with angles smaller than the critical angles undergo total internal reflections and will be guided through the core along the fiber, as shown in Fig. 2.1. The core is typically made of silica doped with germanium or fluorine ($n_{\text{core}} = 1.46$, around 1% higher than that of cladding) and the cladding of silica ($n_{\text{cladding}} = 1.45$ and $n_{\text{air}} = 1.0$).

The numerical aperture (N.A.) of a fiber is defined as the sine of the maximal angle that an incoming ray can have at the fiber input and still be guided. Applying Snell's law on Fig. 2.1 (middle), we have $\cos\theta_c = \frac{n_{\text{cladding}}}{n_{\text{core}}}$ followed by $\sin\theta_I = \frac{1}{n_{\text{air}}}\sqrt{{n_{\text{core}}}^2 - {n_{\text{cladding}}}^2} = n_{\text{core}} \cdot \sin\theta_c \equiv$ N.A.. Thus, technically, a lens with N.A.$\leq \sin\theta_I$ should be used to focus the light into the fiber core and a lens with N.A.$\geq \sin\theta_I$ should be used to collimate the beam coming out of the fiber.

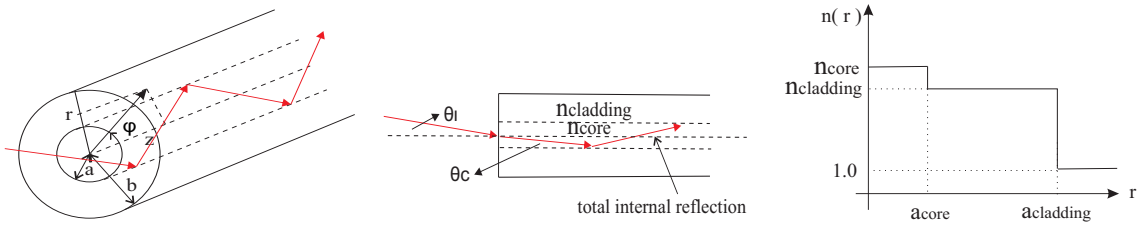

Figure 2.1: (left) A cylinder core-cladding structure optical fiber; (middle) Total internal reflection inside a fiber; (right) The circular step-index profile

Another key factor called V number is defined as V$= \frac{2\pi a}{\lambda}\sqrt{{n_{\text{core}}}^2 - {n_{\text{cladding}}}^2}$. V $\leqslant 2.405$ defines the single mode propagation condition of the fundamental mode for a given wavelength λ and fiber radius a. Normally, a commercial fiber will have a range of wavelengths to work at single-mode propagation. If the wavelength is equal or below the cutoff value, i.e., $\lambda_{\text{cutoff}} \leqslant \frac{2\pi a\sqrt{{n_{\text{core}}}^2 - {n_{\text{cladding}}}^2}}{2.405}$, multi-mode propagation could happen; If the wavelength is too large, the single mode would be poorly confined inside the fiber and there would be loss into the medium outside the fiber.

If we define axis $\widehat{z}$ to be along the fiber axis and solve Maxwell equations under the air-cladding boundary conditions, we will get four sets of propagation modes[2]: the hybrid HE (H_z is larger than E_z) and EH (E_z is larger than H_z) modes, having 6 non-vanishing components of the electromagnetic field ($E_r, E_\phi, E_z, H_r, H_\phi, H_z$ in cylindrical coordinates), and the transverse modes TE ($E_z = 0$ and $E_r = 0$) and TM ($H_z = 0$ or $E_\phi = 0$). The HE and EH modes describe a light wavefront having spiraling propagation in the fiber while the TE and TM modes describe non-rotating trajectories, i.e., propagation in a plane comprising the fiber axis. A **linearly-polarized (LP) mode** is defined to have $|E_z| \ll |E_{r,\phi}|$, which happens when $n_{\text{clad}}/n_{\text{core}} \approx 1$ and θ_c is very small[3].

$$\left(\frac{J_l'(ha)}{haJ_l(ha)} + \frac{K_l'(qa)}{qaK_l(qa)}\right)\left(\frac{(n_1)^2 J_l'(ha)}{haJ_l(ha)} + \frac{(n_2)^2 K_l'(qa)}{qaK_l(qa)}\right) = \left(\frac{l\beta}{k_0}\right)^2\left[\left(\frac{1}{ha}\right)^2 + \left(\frac{1}{qa}\right)^2\right] \quad (2.1)$$

$$h = \sqrt{{n_1}^2{k_0}^2 - \beta^2} \quad , \quad q = \sqrt{\beta^2 - {n_2}^2{k_0}^2} \quad (2.2)$$

The boundary conditions are that the electric and magnetic fields at core-cladding interface are continuous. If the solution of the electric field is assumed to have the form $\vec{E} \propto \exp[-i(\beta z - \omega t)]$, the transcendental equation for solving the propagation constant β is Eq. (2.1). $J_l(x)$, $J_l'(x)$ and $K_l(x)$, $K_l'(x)$ are the first and modified second kinds of the Bessel function and their derivatives respectively. n_1 and n_2 are the refractive indices of core and cladding and a is the core radius while $l = 0, 1, 2, \ldots$. $k_0 = \omega/c$ is the wave vector of the field in vacuum. Also we introduce the definitions

in Eq. (2.2). By numerically solving Eq. (2.1) we obtain a discrete set of values for β, **each of them corresponding to a different propagation mode** in the fiber.

Solving Eq. (2.1) would result in multiple values of β for a fixed l (due to the property of Bessel functions) so we have to introduce another integer m to designate a single specific mode β. The modes are labeled as EH_{lm} and HE_{lm} and two special cases are TM (EH_{0m}) and TE (HE_{0m}) modes. Each mode has its own cut-off V number value, except the HE_{11} mode, which has no cut-off frequency thus is defined to be the fundamental mode. V=2.405, the cutoff value for TM_{01}, is the lowest cutoff value for any non-fundamental mode to propagate inside the fiber. Eq. 2.2 gives the range of the propagation constant: $n_2k_0 \leqslant \beta \leqslant n_1k_0$ since both h and q are positive real numbers. Each mode describes the EM fields in a specific spatial distribution so **a single mode fiber (SMF) carries waves with the same mode but of possible different frequencies**.

2.2 Solution for the fields in tapered nanofibers

I now present the field equations for HE_{11} mode with linear polarization and analyze the evanescent field strength in nanofiber case. The solutions to the Maxwell equations give the $\vec{E}$ field expressions in terms of (r,ϕ,z,t) as in Eqs. (2.3) and (2.4) (More details can be found in [4] or Appendix A in [3].),

$$
\begin{aligned}
&\text{For } r < a,\\
&E_x = -iA\frac{\beta}{2h}\left[(1-s)J_0(hr)\cos\phi_0 - (1+s)J_2(hr)\cos(2\phi-\phi_0)\right]e^{i(\omega t-\beta z)},\\
&E_y = -iA\frac{\beta}{2h}\left[(1-s)J_0(hr)\sin\phi_0 - (1+s)J_2(hr)\sin(2\phi-\phi_0)\right]e^{i(\omega t-\beta z)},\\
&E_z = AJ_1(hr)\cos(\phi-\phi_0)e^{i(\omega t-\beta z)}
\end{aligned}
\tag{2.3}
$$

For $r > a$,

$$
\begin{aligned}
E_x &= -iA\frac{\beta}{2q}\frac{J_1(ha)}{K_1(qa)}\left[(1-s)K_0(qr)\cos\phi_0 + (1+s)K_2(qr)\cos(2\phi-\phi_0)\right]e^{i(\omega t-\beta z)},\\
E_y &= -iA\frac{\beta}{2q}\frac{J_1(ha)}{K_1(qa)}\left[(1-s)K_0(qr)\sin\phi_0 + (1+s)K_2(qr)\sin(2\phi-\phi_0)\right]e^{i(\omega t-\beta z)},\\
E_z &= A\frac{J_1(ha)}{K_1(qa)}K_1(qr)\cos(\phi-\phi_0)e^{i(\omega t-\beta z)}
\end{aligned}
\tag{2.4}
$$

The coefficient A is determined by the normalization condition. For linearly-polarized input, $A = \sqrt{\frac{8\mu_0\omega P}{\pi a^2\beta_{11}}}(D_{\text{in}} + D_{\text{out}})^{-1/2}$. $\frac{D_{\text{in}}}{D_{\text{in}}+D_{\text{out}}}$ and $\frac{D_{\text{out}}}{D_{\text{in}}+D_{\text{out}}}$ are the fractions of the fields power propagating inside and outside the TNF, calculated according to Eq. (2.5) and (2.6). The angle ϕ_0 represents the orientation axis of the field polarization: $\phi_0 = 0$ is x-polarized while $\phi_0 = \pi/2$ is y-polarized.

$$
\begin{aligned}
D_{\text{in}} =& (1-s)\left(1+(1-s)\frac{\beta^2}{h^2}\right)(J_0^2(ha)+J_1^2(ha)) + (1+s)\\
&\left(1+(1+s)\frac{\beta^2}{h^2}\right)(J_2^2(ha)-J_1(ha)J_3(ha)),\\
D_{\text{out}} =& \frac{J_1^2(ha)}{K_1^2(qa)}[(1-s)\left(1-(1-s)\frac{\beta^2}{q^2}\right)(K_0^2(qa)+K_1^2(qa)) + (1+s)\\
&\left(1-(1+s)\frac{\beta^2}{q^2}\right)(K_2^2(qa)-K_1(qa)K_3(qa))]
\end{aligned}
\tag{2.5}
$$

where

$$
\begin{aligned}
s &= \frac{1/q^2a^2 + 1/h^2a^2}{J_1'(ha)/haJ_1(ha) + K_1'(qa)/qaK_1(qa)}\\
h &= (n_1^2k^2-\beta^2)^{1/2}\\
q &= (\beta^2-n_2^2k^2)^{1/2}
\end{aligned}
\tag{2.6}
$$

The squared modulus of the $\vec{E}$ averaged over one oscillation period in the HE_{11} mode inside and outside the TNF is given by Eq. (2.7)[3].

$$|\vec{E}|^2_{\text{in}} = g_{\text{in}}[J_0^2(hr) + uJ_1^2(hr) + fJ_2^2(hr) + [uJ_1^2(hr) - f_pJ_0(hr)J_2(hr)] \times cos[2(\phi - \phi_0)]]$$
$$|\vec{E}|^2_{\text{out}} = g_{\text{out}}[K_0^2(qr) + wK_1^2(qr) + fK_2^2(qr) + [wK_1^2(qr) + f_pK_0(qr)K_2(qr)] \times cos[2(\phi - \phi_0)]] \tag{2.7}$$

where $u = 2h^2/\beta^2(1-s)^2$, $w = 2q^2/\beta^2(1-s)^2$, $f = (1+s)^2/(1-s)^2$ and $f_p = 2(1+s)(1-s)$ while $g_{\text{in}} = |A|^2/2u$, $g_{\text{out}} = |A|^2J_1^2(ha)/2wK_1^2(qa)$. The first and very important step is to get a precise value for the propagation constant β from solving Eq. (2.1) for a specific sub-wavelength optical fiber. Then using the calculated β in Eqs. (2.3) and (2.7) will generate the accurate evanescent field for a specific TNF. In the next section, I will describe the calculated results for our TNF.

2.3 Parameters and fields calculation for our fabricated TNF

In this section, I am calculating the evanescent field and giving some analysis on the results for a sub-wavelength optical fiber with parameters: fiber radius $a = 179$nm, wavelength used $\lambda = 780$nm, refractive indexes $n_1 = 1.45$ and $n_2 = 1.0$. Solving Eq. (2.1) gives the propagation constant $\beta = 8.6 \times 10^6 \text{m}^{-1}$. In Fig. 2.2(a), I plot the cross-section of the total electric field intensity for the HE_{11} mode with the initial polarization $\phi_0 = 0$ (x-polarized). The field has obvious discontinuity at the fiber-air boundary and asymmetric profiles along x and y. In Fig. 2.2(b) and Fig. 2.2(c), I plot the cross-section of the field inside and outside the fiber respectively. Fig. 2.3 shows that the evanescent field along x is much stronger than that along y but also decays much faster.

In Fig. 2.4, I calculated and plotted the variation of $|E(r = a, \phi = 0)|^2_{\text{out}}$ as a function of a/λ using the same parameters as above. The calculations have been performed assuming the x-polarized electric field and the magnitude $|E|^2_{\text{out}}$ is evaluated at $(r = a, \phi = 0) = (x = a, y = 0)$, thus the polarization of the $\vec{E}$ field is perpendicular to the fiber surface, in which case the evanescent field is optimal. The $|E|^2_{\text{out}}$ reaches its maximum at a fiber radius of $a = 0.23\lambda \approx 179.46$nm. In general, for silica fibers, a significant evanescent field appears when $a/\lambda < 0.5$. As the fiber radius is reduced, $|E|^2_{\text{out}}$ first increases to its maximum then starts decreasing because the mode diameter

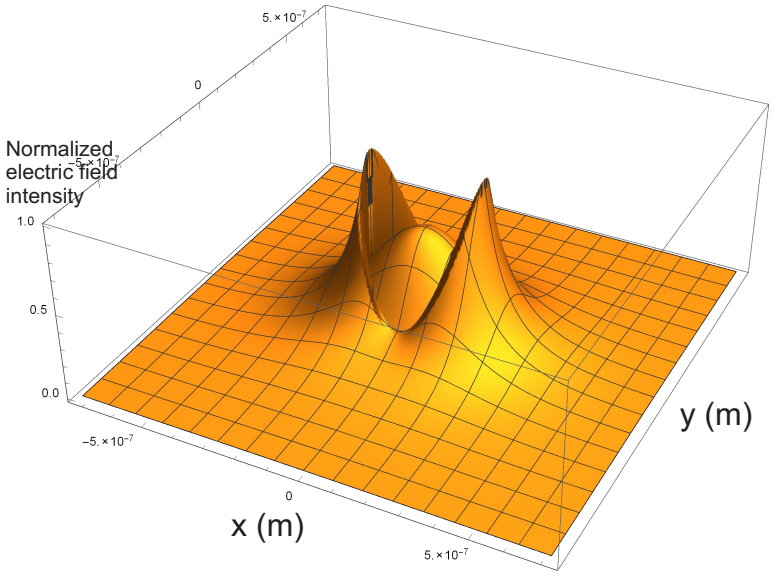

(a)

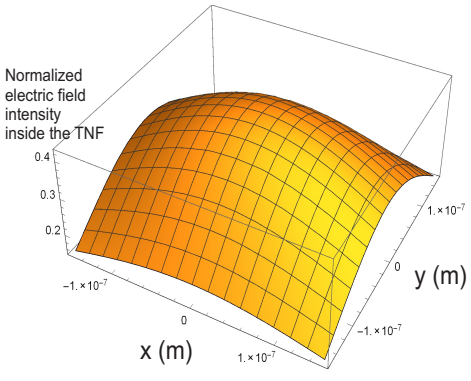

(b)

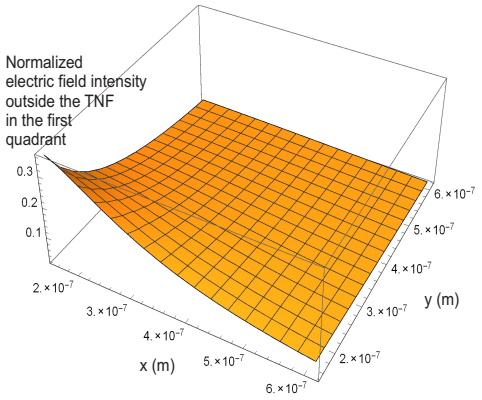

(c)

Figure 2.2: (a) Cross-section profile of the normalized total electric field intensity; (b) Normalized electric field intensity inside the fiber; (c) Normalized electric field intensity outside the fiber for the HE_{11} mode with linear polarization at the input; Parameters used for the figure demonstration: $a = 179$nm, $\lambda = 780$nm, $n_1 = 1.45$, $n_2 = 1.0$, propagation constant $\beta = 8.567 \times 10^6 \mathrm{m}^{-1}$ and $\phi_0 = 0$.

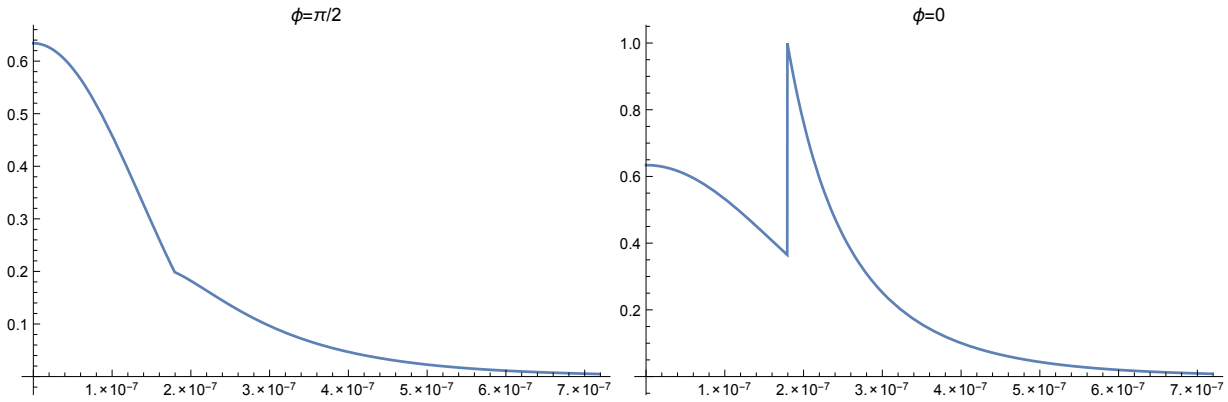

Figure 2.3: (left) Total field intensity as a function of y (x=0, $\phi = \pi/2$); (right) Total field intensity as a function of x (y=0, $\phi = 0$); Parameters used for figure demonstration are the same as in Fig. 2.2.

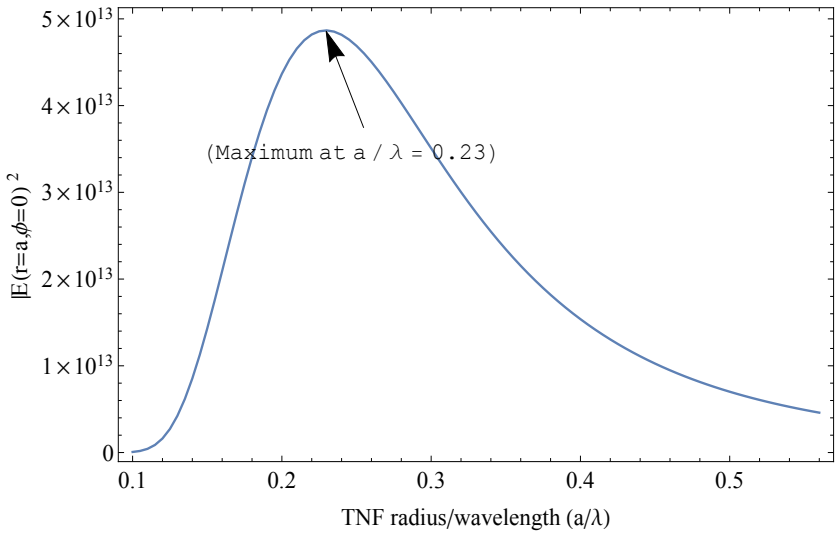

Figure 2.4: $|E(r = a, \phi = 0)|^2_{\text{out}}$ as a function of the ratio a/λ assuming x-polarization of the transverse field (Eq. 2.4)

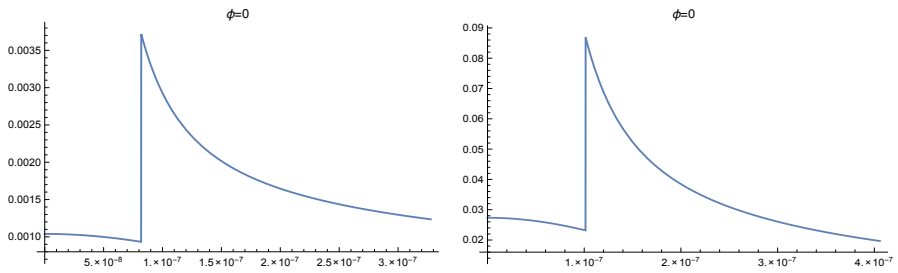

(a) a/$\lambda = 0.105$

(b) a/$\lambda = 0.130$

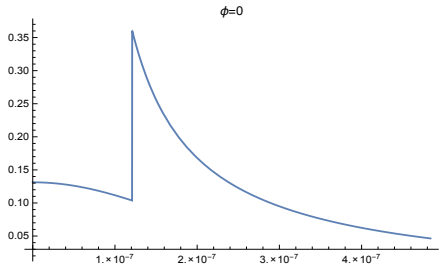

(c) a/$\lambda = 0.155$

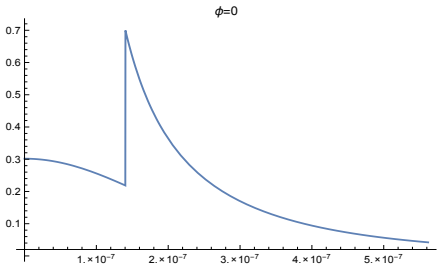

(d) a/$\lambda = 0.180$

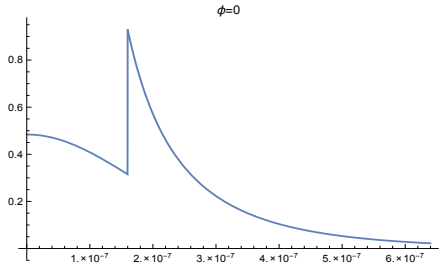

(e) a/$\lambda = 0.205$

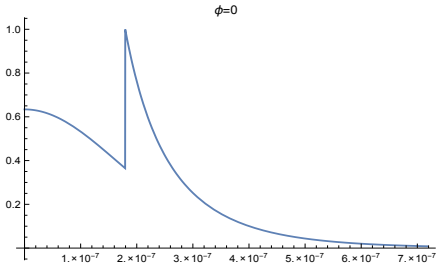

(f) a/$\lambda = 0.230$

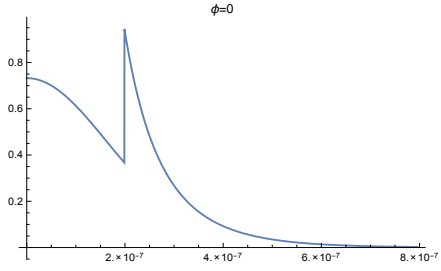

(g) a/$\lambda = 0.255$

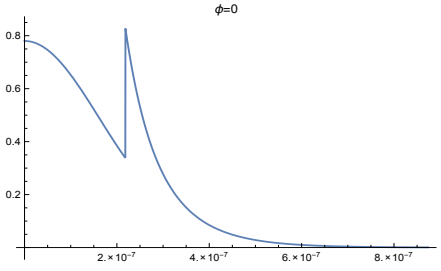

(h) a/$\lambda = 0.280$

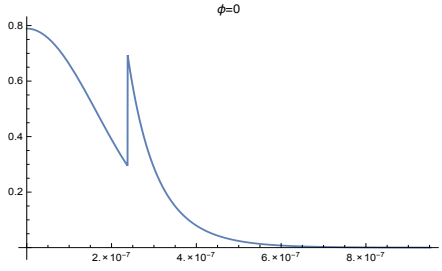

(i) a/$\lambda = 0.305$

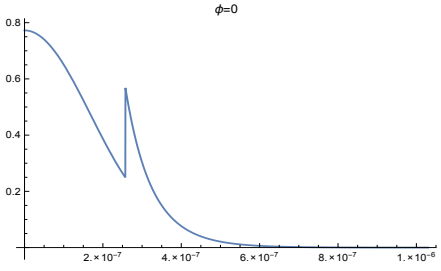

(j) a/$\lambda = 0.330$

Figure 2.5: Variation of $|E(r,\phi=0)|^2_{\text{out}}$ normalized to its maximum value at a=0.23λ for x-polarized light as a function of the ratio a/λ

Company, Part number	OZ Optics, SMF-633-4/125-0.25-NF-L
Operating Wavelength	600-850nm
Cutoff Wavelength	$<$600nm
Core Diameter	4.0μm
Cladding Diameter	125$\pm$2μm
Jacket Diameter	0.25mm
Numerical Aperture	0.10-0.13
Cladding refractive index	1.453 @ 780.24nm

Table 2.1: Specifications of our single-mode fiber used for pulling

keeps increasing, in which case the $\vec{E}$ field gradually transforms into a plane wave and the fiber will not be able to radially confine the light anymore. I am showing this evolution in Fig. 2.5, in which $|E(r,\phi=0)|^2$ normalized to its maximum value $|E(r=a,\phi=0)|^2_{\text{out},a=0.23\lambda}$ is plotted as a function of a/λ. For small values of a the field guiding is weak while for large values of a the field is mostly guided inside the fiber and the evanescent field is small.

The knowledge of the evanescent field strength at the fiber vicinity is very important in quantum optics experiments where dipole emitters are coupled to the light field. The parameters used in the above calculation and demonstration correspond to the experimental work described in this thesis: ^{87}Rb atoms interacting with 780.246nm evanescent field around an ultra-thin optical fiber with optimal radius 179.46nm. However, certain experimental limitations have to be taken into consideration when choosing the appropriate fibers for experiments, for example, the total transmission through the fiber in the pulling process or its mechanical properties. In the next section, I will describe our fiber pulling procedure in detail as well as how we make sure to approach this optimal radius in our TNF fabrication.

2.4 Fabrication of ultra-thin tapered nanofibers

Our TNF is fabricated in Professor Paul Barclay's nanophotonics lab using flame brush technique. The specifications of the single mode fiber used for fiber pulling are given in Table 2.1. The

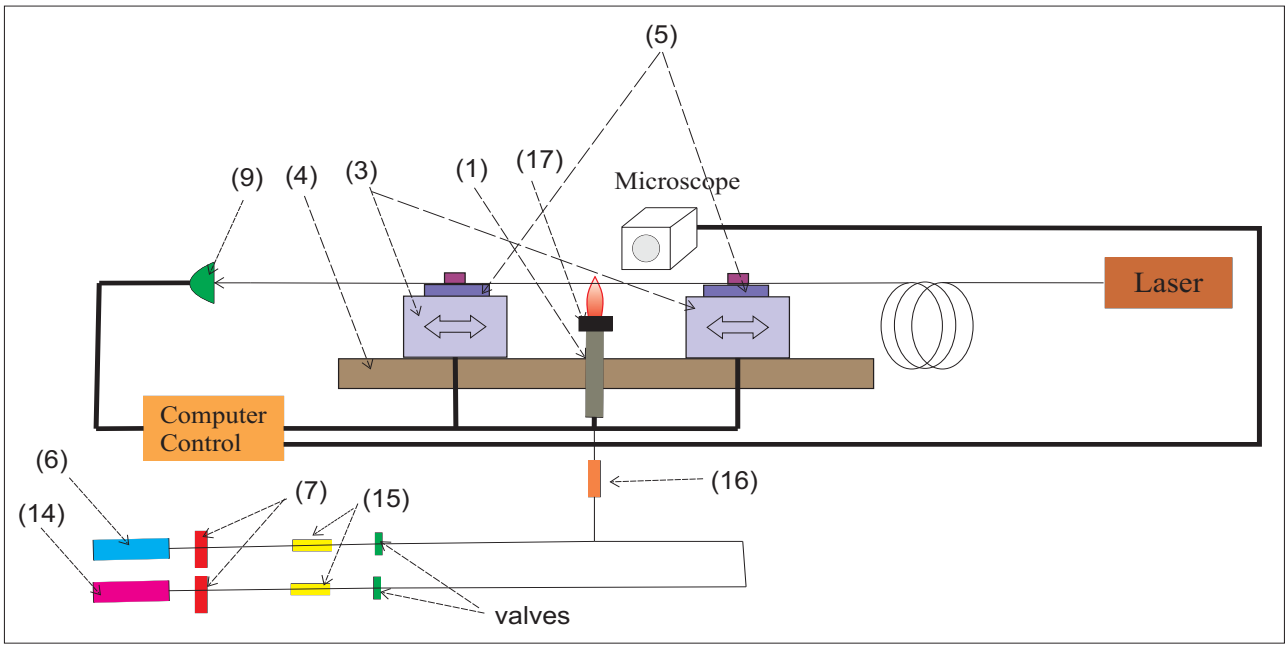

Figure 2.6: A side-view scheme of our fiber pulling setup (Not all of the parts are displayed.)

construction of our fiber pulling setup is going through two stages: The old fiber pulling setup used hydrogen as the only flame gas and the new scheme, as shown in Fig. 2.6, adds oxygen to generate the flame. The list of equipment parts is given in Table 2.2 with numbers corresponding to Fig 2.6 (Not all of them are displayed).

Interested readers can refer to Appendix A for a fiber pulling procedure. Basically, there is a heater (in our case a oxyhydrogen flame) keeps heating a portion of a standard single mode optical fiber while a pair of computer-controlled motorized fiber-pulling stages gradually pull both ends of the fiber. The transmission of a fiber pulling is defined to be the final optical power measured at the end of pulling divided by the initial optical power measured before pulling. We want this ratio to be as close to 100% as possible, which means that the whole pulling process does not result in much loss. A high transmission also indicates a high quality fiber because the fiber, in this case, is being pulled very adiabatically (Interested readers can refer to [5] or [19] for adiabatic analysis) and any loss through this tapered fiber is negligible.

The simplest case is that the heater stays static and the motors move away from each other in a

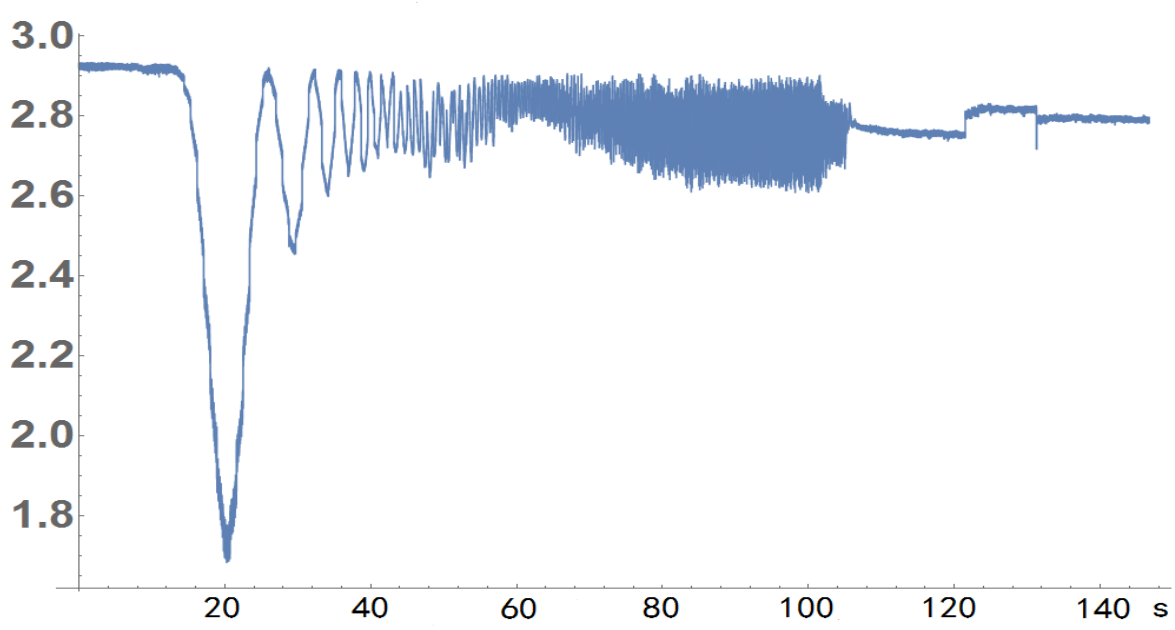

Figure 2.7: A 95% fiber pulling profile: transmission amplitude as a function of pulling time (every 5000 tracing points is 1s)

constant speed, which we call "non-dither" pulling. The best parameters we found for this type of pulling to allow a highest transmission using our setup are given in Table 2.3. A more complicated pulling process allows the heater to move back and forth with regard to the fiber (In the real case, the motors are moving back and forth with different speeds without moving the flame.) so that more points on the fiber can be heated up and a longer tapered waist can be obtained. An algorithm is recommended for what we call "dither" pulling to make sure that every single point on the fiber is swept by the flame for the same amount of time so that adiabaticity can be optimized. We are still in an optimization process using the oxyhydrogen flame. Up to the time of finishing this thesis, we found that 45mL/min for O_2 and 90mL/min for H_2 (from the new flow meters) might be a good choice and a 87% transmission pulling is reproducible. Some parameters we are using for "dither" pulling can be found in Table 2.4. In the next section, I will talk in detail about our fiber pulling algorithm. Finally, we used both SEM and diffraction-based measurements [6] to get the estimation of the TNF waist thickness and the results are consistent.

From the calculation in section 2.2, the evanescent field magnitude $|\overrightarrow{E}(x, y=0)|^2_{\text{out}}$ reaches

	Item Part	**Description**
(1)	National Torch 3H hydrogen	Part number 34-10099, 7 stainless steel elbow and has 3/8-24
(2)	National Torch tip HT-3 series	Product number 34-10168, Silent Burn, .025" x 31 orifices
(3)	Two computer-controlled motorized translational stages	Suruga KXL06050-C1-C
(4)	Stepping motor controller	Suruga DS102MS
(5)	Two rotating fiber clamps from Thorlabs	Model number HFR007 (fix the bare fiber onto translational stages)
(6)	Hydrogen gas cylinder from Praxair	Purity 4.5
(7)	National gas regulator	maximum outlet pressure 60 psi
(8)	Volume-based gas flow meter	from Cole Parmer
(9)	Visible photodetector from New Focus	Model number 1621 (to monitor fiber transmission)
(10)	UV glue to fix the tapered fiber onto the bracket	Dymax OP-4-20632
(11)	UV lamp to cure the UV glue	Dymax Bluewave 75 UV Curing Spot Lamp with Intensity Adjustment
(12)	Fiber cleaver from Ericsson	Model number EFC 11
(13)	Fiber fusion splicer	Ericsson FSU 995 FA
(14)	Oxygen gas cylinder from Praxair	Purity 5.0, cylinder fill pressure 2200 psig, gas volume 6.90m^3, Part number OX 5.0RS-K
(15)	Swagelok SS-4F-7	Particulate filter, 7μm pore size
(16)	GLFPF3000SM4	"Mini Gaskleen filter" from PALL
(17)	Custom SS nozzle	29, 200μm holes in a 1x2mm^2 array
(18)	Volume-based gas flow meters (two)	Model FM-1050 Series from Matheson

Table 2.2: List of equipment parts for the fiber pulling setup with numbers corresponding to Fig. 2.6 (Not all of the parts are displayed.)

Laser wavelength used for pulling	636∼640nm
Optimal hydrogen flow rate	295mL/min (from the old flow meter)
The optimal relative speed between the two motors	70 pulses/s$\times$2μm/pulse=140μm/s
Flame z-direction movement	865∼875 (optimization required)
Flame height	around 5.73mm (optimization required)
Approximate pulling duration	2∼3mins
Maximum transmission	98% (typically 85%∼98%)
TNF waist thickness	350-460nm
Total length including waist and transition parts	1.2cm

Table 2.3: Some fiber pulling and TNF characteristic parameters for non-dither pulling

Laser wavelength used for pulling	636∼640nm
Optimal hydrogen flow rate	345∼350mL/min (from the old flow meter)
The optimal relative speed between the two motors	140μm/s (1430 and 1500pps)
Flame z-direction movement	865 (optimization required)
Flame height	5.73mm (optimization required)
Approximate pulling duration	4.5∼5mins
Maximum transmission	94% (typically 85%∼94%)
TNF waist thickness	350-460nm
TNF waist length (linear)	2∼3mm

Table 2.4: Some fiber pulling and TNF characteristic parameters for dither pulling

its maximum value at TNF radius $a = 0.23\lambda$, which is 358.8nm in diameter for 780nm laser in our experiments. This means that the desired fiber waist for our pulling should be around this value. Since the final radius is proportional to the pulling wavelength through $a = \frac{2.405\lambda}{2\pi\sqrt{n^2-n^2_{air}}}$, the thinnest diameter we can reach in our pulling is around 460nm using a visible 630nm fiber coupled diode laser.

As an example, a fiber pulling profile of the transmission is shown in Fig. 2.7. A fiber pulling profile is the signal collected by a computer from the output of a photodetector, which is connected to the end of the fiber during pulling to measure the transmission of a laser through the fiber. The reason for doing this is that during heating and pulling, the structure of the original fiber is highly modified and monitoring the optical signal passing through the fiber is an effective way to evaluate the stage of pulling and the best time to stop pulling. We can see from Fig. 2.7 that, in the first 12s, the fiber is being heated up but the fiber core is still intact so the wave propagation is still in a single mode; A significant drop in transmitted power at 16s indicates that the fiber core starts being destroyed and melted into the cladding; At this moment, the fiber at the tapered part can not be treated as a single mode fiber any more because the diameter of the melted fiber is larger than the original diameter, i.e., 4μm so multi-mode propagation appears. Beating signals due to interference between different modes dominate the transmission until around 108s when all the oscillations suddenly stop. This indicates that the fiber is being pulled down to a diameter that satisfies the only fundamental mode propagation condition again and this is the right time to stop pulling. The laser used here is 633nm and the transmission is around 95% while having a fairly clear single mode spectrum. After a TNF is available, it is extracted[6], transferred to our lab and put into the UHV system.

Some improvement to the fiber pulling setup Our fiber pulling setup was constructed around four years ago and degradation happens with time thus the reproducibility of producing the same quality nanofiber with the same parameters, i.e., hydrogen flow rate, flame height, pulling speed/acceleration, is getting worse. After years of using, the nozzle may need replacing due to the oxidization ("sug-

aring") of the stainless steel. We have already fabricated a new one and we took a lot of reference from Dr. Steve Rolston's group at University of Maryland and we have been going through a lot of helpful discussion with people working there. **First**, we are trying a new nozzle with micron size holes, which is said to help improve the flame stability close to the nozzle as well as offer a safer precaution to avoid the hydrogen backflow into the gas lines. **Second**, we are adding oxygen to the gas line. It is pointed out on one hand that adding oxygen is a necessary step to form a stable and well-defined flame since using the ambient gas for combustion led to a very "nebulous" kind of flame that is not as stationary or well-formed. Moreover, controlling the ratio of hydrogen and oxygen will give the freedom to tune the temperature of the flame to the desired value. On the other hand, it is also pointed out[8] that the high pressure jets of hot gases from adding oxygen would make the flame much more "violent". **Finally**, one has to keep in mind that the pulling quality and reproducibility are affected by many other factors as well: precise fiber pre-alignment, fiber-flame distance, pre-pull cleanness etc.. We are replacing the current volume-based measurement flow meters with better ones. The differences in the setup configuration and specific components are shown in both Fig. 2.6 and Table 2.2.

Another issue that is worth of mentioning here is the cleaness of the fiber: the pre-pull cleaning, the maintenance of cleanness during and after pulling. TNF transmission is very sensitive to its cleanness and its degradation with the increase of the surface pollution has been widely investigated ([9] and [10] for example). In Fig. 2.8, we give an example of transmission degradation as the amount of dust increases with time. We can see the dust from microscope (top figure) and the transmission degradation rate is around 5.89% per min (the first slope in the bottom figure). At around 12 minutes, we dropped isopropyl alcohol (IPA) on the TNF to remove part of the dust, but it did not help the transmission recover to the original value and the degradation after this seems to be even faster. Thus having a clean enough pulling environment for fiber pulling is crucial. The lower the transmission is, the easier it is to burn the fiber in the UHV environment due to the lack of thermal conduction while the dust keep absorbing energy from the evanescent field and heating

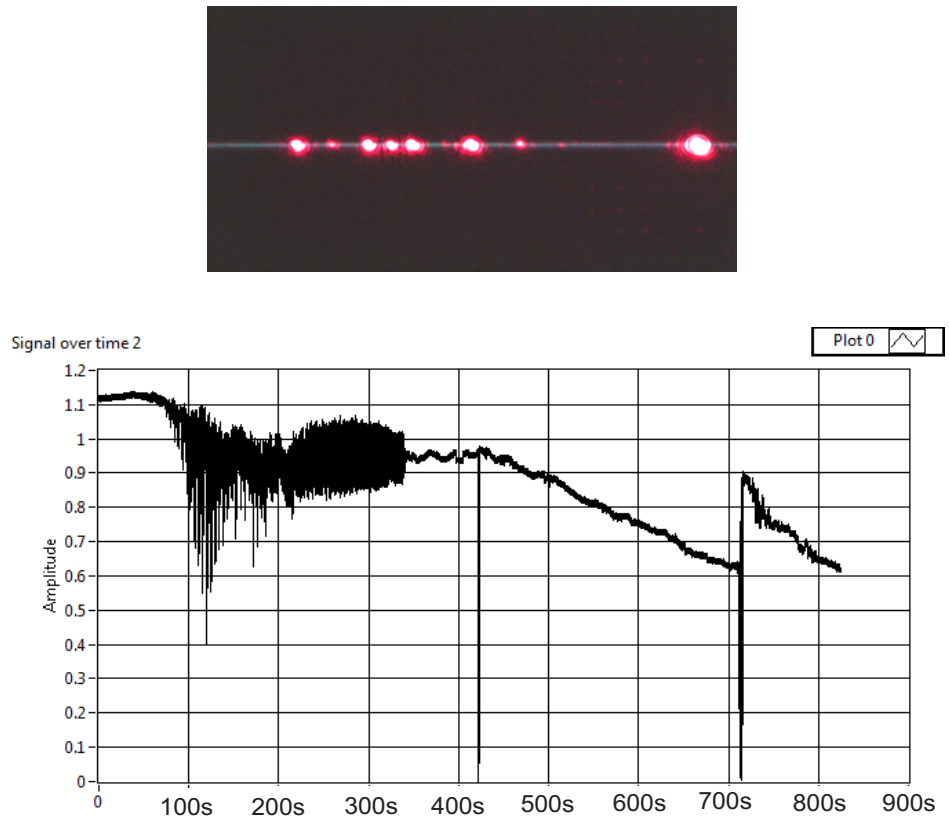

Figure 2.8: (top) A fiber with dust on it under microscope; (bottom) A degradation example from a 84.8% fiber pulling: transmission amplitude as a function of pulling time (every 5000 tracing points is 1s)

up the fiber. We have been struggling with this fiber burning issue for a long time and we are still working on it to improve the cleanness of the fiber pulling environment. For example, we are installing a flowbox on top of the whole fiber pulling setup and wrapping everything around with strip curtains, which will allow a good air-sealing condition. We also have to find a way to speed up our fiber extraction process so that fewer or even no dusts would fall onto the TNF during this procedure.

2.5 Fiber pulling algorithm

We first define all our variables and parameters. As shown in Fig. 2.9, the radius of the untapered fiber is r_0. L is the length of the fiber being heated by the heating source so it is changeable under

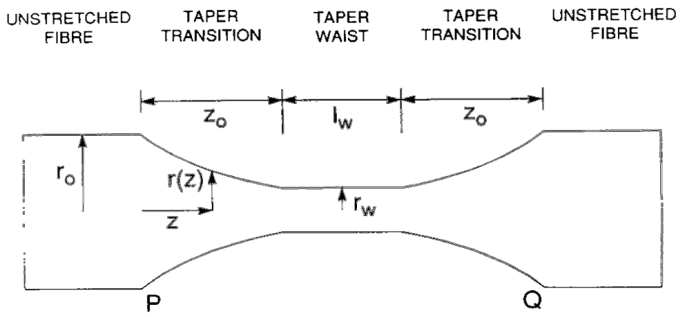

Figure 2.9: The structure of a fiber taper [5] with parameters defined at the end of pulling

the control of the heating source. We use δL to represent its change and L_0 its initial value at the beginning of pulling. z axis is along fiber and $z = 0$ is at point P. During pulling, the taper extension, x, is the net distance through which the taper has been stretched. For example, if the distance PQ at time t_1 is pulled to a new distance P'Q' at time t_2, x =P'Q'-PQ. The change in x is δx and the change in time is δt. A few more parameters are defined to describe the tapered fiber shape: l_w and r_w are the length and radius of the uniformly tapered waist, z_0 is the length of the taper transition and its shape is described by a decreasing local radius function $r(z)$. The final extension when the taper is finished and elongation stops is denoted by x_0.

2.5.1 The forward problem

$$\pi(r_w + \delta r_w)^2(L + \delta x) = \pi {r_w}^2 L \tag{2.8}$$

$$r_w(x) = r_0 \exp(-\frac{1}{2}\int_0^x \frac{dx'}{L(x')}) \tag{2.9}$$

In the forward problem, L as a function of x and x_0 are given, and l_w, r_w, z_0, $r(z)$ are required. The rule of thumb is that during pulling, the mass or the glass volume is conserved. In Fig. 2.9, the volume between points P and Q at time t equals to that at time $t + \delta t$ gives us the relationship in Eq. (2.8) (Here we neglect the small difference between the core and cladding densities.). Writing out the left side and ignoring the second order terms reduces it to $\frac{dr_w}{dx} = -\frac{r_w}{2L}$. Now the variation of the waist radius with taper elongation can be obtained through simply

integrating the above expression on both sides with the initial condition $r_w(t=0)=r_0$, which is $\int_{r_0}^{r_w}\frac{dr'_w}{r'_w}=-\frac{1}{2}\int_0^x\frac{dx'}{L(x')}$, giving a general expression in Eq. (2.9). Thus in a forward problem, given the heating source information $L(x)$, we can calculate $r_w(x)$ for any time point.

$$r(z)=r_0e^{-z/L_0} \tag{2.10}$$

The simplest example is a constant hot-zone heating source, in which $L(x)=l_w=L_0$. In this case, Eq. (2.9) will become $r_w(x)=r_0\exp(-x/2L_0)$. Considering the full taper extension x is twice of a single side extension z, i.e., $x=2z$, we will have the final expression as shown in Eq. (2.10), which is the result found elsewhere. Reference [5] analyzes the results for a linearly changed hot-zone heating source and a more complicated distance law needs to be substituted into the integral to find $r(z)$.

2.5.2 The inverse problem and a fiber pulling algorithm

In the inverse problem, l_w, r_w, z_0, $r(z)$ are given, L as a function of x and x_0 are required. The volume law $\frac{dr_w}{dx}=-\frac{r_w}{2L}$ can be rewritten as $\frac{dr}{dx}=-\frac{r}{2L}$. The other law we are using here is the distance law. Suppose that initially a piece of fiber with length L_0 and $x/2$ length on each side is being pulled and at time t, we only have a uniformly tapered part L and two identical transition parts with length z filling this distance, the distance law states that $L_0+x=L+2z$. Its differentiation over r gives $\frac{dx}{dr}=2\frac{dz}{dr}+\frac{dL}{dr}$. Together with the volume law we have a first-order linear differential Equation 2.11 for L as a function of r (dz/dr is assumed to be known in an inverse problem since $r(z)$ is given.).

$$\frac{dL}{dr}+2\frac{L}{r}+2\frac{dz}{dr}=0 \tag{2.11}$$

Solving this equation with initial condition $r=r_0$ and $L=L_0$ at $z=0$ gives L's expression in terms of $r(z)$, r_0 and L_0. L_0 can be evaluated then by the condition that $L(z_0)=l_w$ when $z=z_0$ at the end of the pulling. Up to this point, we can express L in terms of $r(z)$, r_w, l_w and z_0, which

are all known quantities. Finally, evaluating the distance law $x(z) = 2z + L(z) - L_0$ at $z = z_0$ gives $x_0 = 2z_0 + l_w - L_0$, which together with L constitute the complete solution of this inverse problem.

A fiber pulling algorithm We are implementing an algorithm in our fiber pulling, which we learned from Professor Steve Rolston's lab at University of Maryland[7] and I am briefly summarizing the main idea here. In a non-dither pulling process, the flame stays stationary so the effective heating zone is constant while the motors are moving away from each other. The tapered fiber shape, as derived in the last section, is an exponentially decreasing function. In this case, the uniform waist length l_w is actually zero because two identical exponential parts connect directly to each other. However, having a longer tapered waist length could benefit a lot of experiments. As stated in Chapter 1, the optical depth of the light-atom nonlinear interaction is proportional to the interaction length, which here is how long the nanofiber could guide the evanescent field in a uniform strength. To get a longer tapered waist length, dither pulling is necessary (what we call "flame brushing" technique).

As two motors are moving away from each other, the flame is also moving back and forth along the fiber axis to allow a part of the fiber longer than the heating zone to be heated. In the real implementation, dithering torch gives too much disturbance to the flame so instead, different velocities are given to the motors to realize this without really moving the torch. However, compared to non-dither pulling, this process could be much less adiabatic without any algorithm[5]. To have an optimal adiabatic pulling, an algorithm is necessary to calculate the required movement parameters precisely before pulling based on the desired taper parameters, as well as to keep controlling the movement during pulling. The details about this algorithm and the code can be found in reference [23]. Basically, in this algorithm, the tapered fiber is treated as a series of small fiber sections that are well approximated by lines and the resolution is determined by the sampling number chosen in the code. The transition part is a linear part with a given slope and it connects to an exponential section that smoothly reduces and connects to the uniformly tapered section. To accommodate this adiabatic change, the algorithm divides the pulling into several steps, each of which has its specific

pulling velocity and dither time.

$$\frac{r_n}{r_{n-1}} = \exp(\frac{-t_{0,n}v_n}{2L_0}) \tag{2.12}$$

The volume law restricts the ratio of radii r_n and r_{n-1} in two adjacent pulling steps n and $n-1$ as in Eq. 2.12, where $t_{0,n} = \frac{L_0}{v_n}\ln(\frac{2v_h+v_n}{2v_h-v_n})$ is the time during which the flame fully sweeps a single point on the fiber and v_n is the relative velocity at which the two motors are moving apart in step n. v_h is the dithering velocity of the flame. L_0 is the length of the heating zone, which can be predetermined by doing a non-dither pulling and fitting the radii data to the exponential Eq. (2.10).

$$r_{n-1}^2 L_{w,n-1} = r_n^2 L_{w,n} + r_{n-1}^2(v_h - \frac{v_n}{2})t_{0,n} \tag{2.13}$$

$$(L_n - v_h t_{0,n})(v_h - v_n/2) = v_h L_{w,n} \tag{2.14}$$

The algorithm recursively calculates the parameters $t_{0,n}$ and v_n, starting from the desired final radius r_w, until reaching the initial radius r_0. The volume law also relates the tapered waist lengths in two adjacent steps, $L_{w,n}$ and $L_{w,n-1}$, as in Eq. (2.13). Finally Eq. (2.14) is used to determine the distance the flame has to sweep in step n, i.e., L_n, to calculate the new velocity v_n for the next step. Interested readers are recommended to read reference [7] for a more comprehensive analysis and demonstration.

2.6 Investigation on TNF thermal dynamics through interferometry

Thermalization via heat radiation is generally an interesting topic in physics and there has been a lot of investigation on macroscopic bodies described by Planck's law. However, when the size of an object is comparable to or even less than the thermal wavelength, a more comprehensive theory is recommended to use. A few approaches, for example, fluctuational electrodynamics (FED), have been proposed to analyze this case by considering the Casimir forces and the radiative heat transfer in both far- and near-field. In 2013, Rauschenbeutel's group[11] published a paper in Physical

Review Letters about their investigation on the thermalization dynamics of their predetermined size and shape nanofibers. It has both theoretical simulation based on FED and experimental measurement of their fiber thermal expansion using a TNF coupled Fabry-Perot-type optical resonator. Here we did a similar experiment on our nanofiber in a different way. Another motivation behind this investigation is that some research shows that raising up the TNF temperature can generate atomic evaporation, which can preserve the fiber transmission and extend its lifetime[10]. Using a laser for this purpose might be a convenient way to diagnose our fiber quality.

We employ a silica nanofiber with a diameter around 400nm and monitor its temperature-dependent optical path length in an interferometric way during heating and cooling. The fiber resides in an ultrahigh vacuum chamber $\sim 10^{-8}$torr. A temperature change of its waist induces a change in the optical path length. By switching the heating laser beam with a mechanical shutter, the heat source can be turned on and off, allowing us to measure the heating and cooling dynamics of the nanofiber. According to reference [11], experimentally, they found that the heat diffusion through the surrounding background gas is negligible for pressures below 10^{-4}torr, which is consistent with our experiment. Here, we did this investigation over a limited temperature range compared to [11] due to the "burning fiber" problem we mentioned in section 2.4.

Fig. 2.10 shows our experimental schematic. We are measuring the change in the phase due to the change in the optical path during heating/cooling through optical and electronic heterodyne detection. The probe laser is split into a strong beam used as the optical local oscillator (LO, around 7$\sim$9mW) and a weak signal beam (around 25μW), which passes through an acousto-optic modulator (AOM, 65MHz central frequency) twice so the heterodyne beating signal at the homodyne detector (HD) is 130MHz. To get the phase information from this signal, we generate an electronic LO at 130MHz+100Hz and combine it with the 130MHz signal at a frequency mixer (ZX05-1L-S+, 2$\sim$500MHz). Low pass filters (LPF, $f_c \approx$ 100MHz) are used at some steps to exclude the higher order harmonics to make sure that we get a clean 100Hz signal at the output. Finally, a 100Hz phase-synchronized signal and its 90° conjugated signal are used as reference signals to

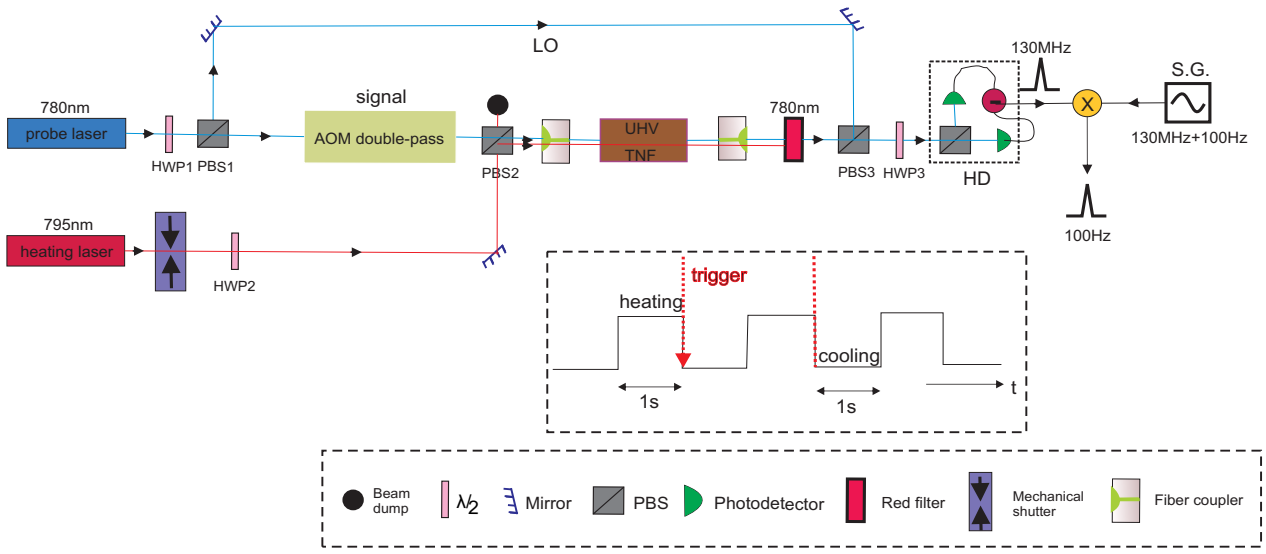

Figure 2.10: A simplified experimental schematic of the TNF temperature measurement through heterodyne interferometry and the timing series used

multiply with the 100Hz signal to obtain its two quadratures.

This experiment mainly uses interferometry for the measurements. A HD is used in the first step as an optical interferometer. The weak 25μW signal beam interfering with a strong LO beam of 7mW generates a beating signal with power around $A \approx$-11dBm $\sim$ -15dBm and the frequency is ω_1 =130MHz. We can represent this signal simply by $A\cos(\omega_1 t + \phi_{TNF} + \phi_n)$, in which ϕ_{TNF} is the phase change due to heating and ϕ_n is the phase noise due to other experimental components in the free space. To precisely synchronize the reference signal and the experimental signal, we are actually performing an electronic heterodyne interferometry as well. We first use a Direct Digital Synthesizer (DDS) to generate a signal at frequency ω_2 =130.0001MHz and split it into two channels: one of them, around 2dBm, $B\cos(\omega_2 t)$, is sent into the frequency mixer with the signal coming from the HD to get an interferometric electronic signal at ω_3 =100Hz after a LPF at 100MHz, i.e., $\frac{AB}{2}\cos(\omega_3 t - \phi_{TNF} - \phi_n)$; The other one, is sent into a second frequency mixer with a direct 130MHz signal from the DDS to generate a reference signal at the output: $C\cos(\omega_3 t)$. Then both of this reference signal and the experimental signal are sent to a digital oscilloscope for their multiplication: $\frac{ABC}{4}\cos(\phi_{TNF} + \phi_n)$. The oscilloscope also generates a 90° phase-shifted reference

signal from the original reference signal, $C\sin(\omega_3 t)$, used to multiply with the experimental signal as well. We get $-\frac{ABC}{4}\sin(\phi_{TNF}+\phi_n)$, which helps eliminate the uncertainty of $\phi_{TNF}+\phi_n$ from inverting only one quadrature function. We processed data in Mathematica and the average over the phase noise is assumed to be zero: $\bar{\phi_n}=0$ so we can extract the phase information ϕ_{TNF} due to heating up the tapered fiber and analyze its dynamic thermalization as described in the following part.

All the synchronized signals are generated from an AD9959 200MHz DDS signal generator and the phase-shift as well as the multiplications are done by a digital oscilloscope we used for data collection. We took data with a sampling rate 5000 sampling traces/s and each data file is 2s, including 1s heating and 1s cooling. The mechanical shutter is synchronized to the oscilloscope through a trigger signal generated from a Vc++ program on the lab computer. For a given heating power, the experiment (1s heating and 1s cooling, i.e., no heating, and here we assume that the process for reaching equilibrium takes a few ms.) is repeated for 300 times and the data is stacked/averaged so that the SNR is increased by $\sqrt{300}\approx 17.32$. Fig. 2.11 shows the extracted phase information in radians as a function of time for heating powers ranging from 0 to 700μW while Fig.2.12 shows the results for heating powers ranging from 1 to 4.5mW. In all these figures, the horizontal axis is 5000 sampling points, which correspond to 1s and the vertical axis shows the phase change in radians. The heating power is given below each figure and the blue curve represents the heating process while the yellow curve represents the cooling process, in which the heating laser is blocked by a mechanical shutter. The expected change trends in phase due to heating and cooling are opposite and the discrepancy observed in our experiments are explained below.

The physics behind investigating the optical path length change are the thermal-optic and the strain-optic effects of silica: its refractive index n depends on its temperature and strain as well as the radial thermal expansion of the fiber. All of these effects will lead to the change of the V number of the vacuum-cladding fiber waist, $V=2\pi a\sqrt{n^2-1}/\lambda_0$, either via a change of n or via a

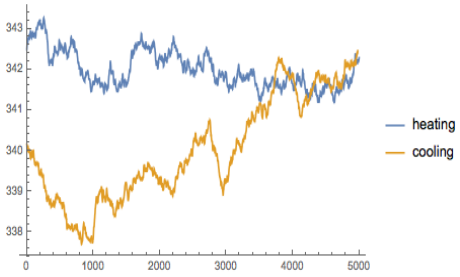

(a) power = 0μw

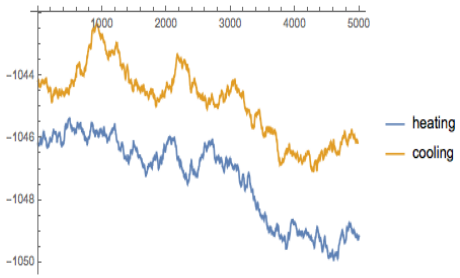

(b) power = 300μw

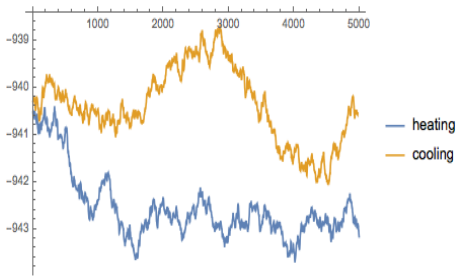

(c) power = 400μw

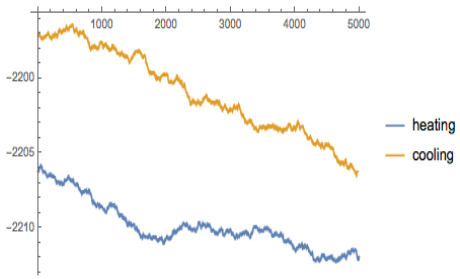

(d) power = 500μw

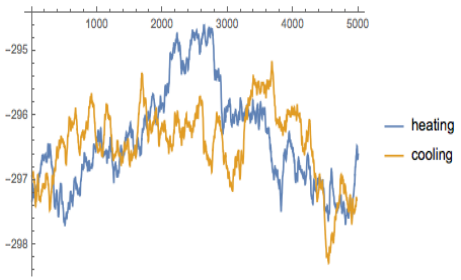

(e) power = 600μw

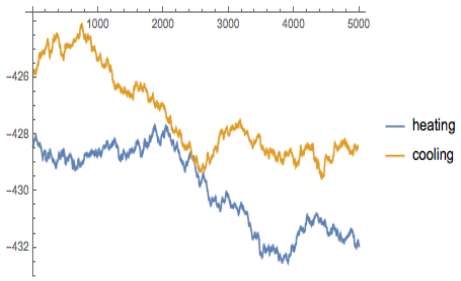

(f) power = 700μw

Figure 2.11: The extracted phase information (in radians) as a function of time between 0∼1s (5000 sampling traces) for low heating powers up to 700μW. The blue curve is in heating process while the yellow curve is in cooling process.

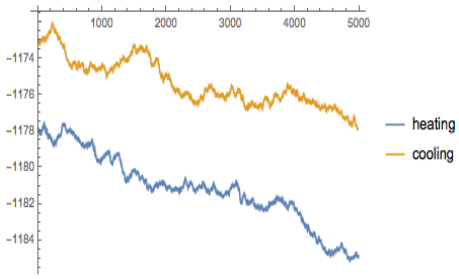

(a) power = 1mw

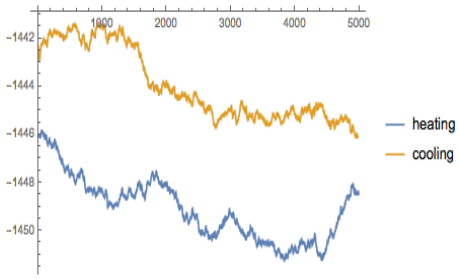

(b) power = 1.5mw

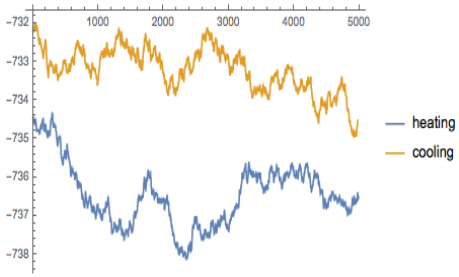

(c) power = 2mw

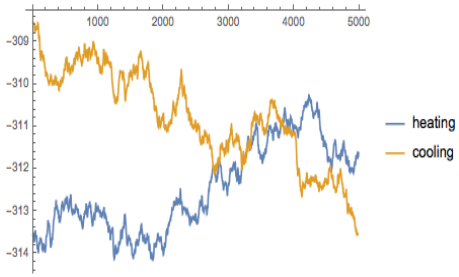

(d) power = 2.5mw

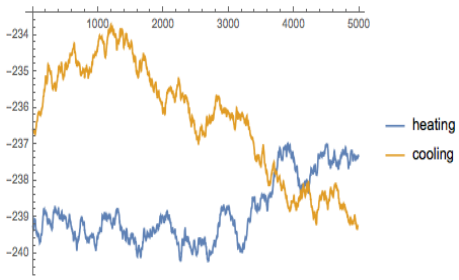

(e) power = 3mw

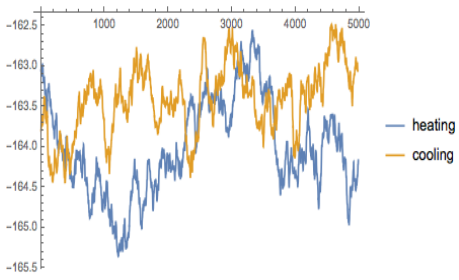

(f) power = 3.5mw

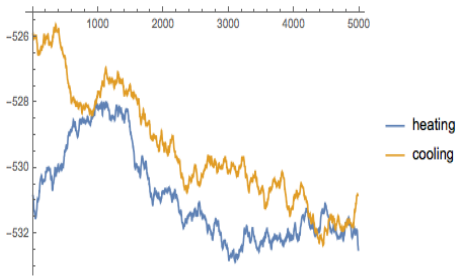

(g) power = 4mw

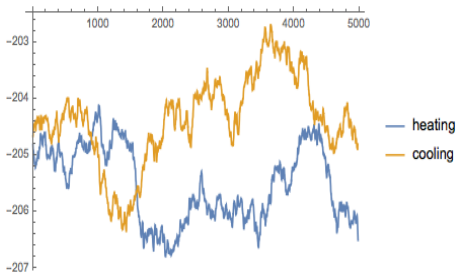

(h) power = 4.5mw

Figure 2.12: The extracted phase information (in radians) as a function of time between 0∼1s (5000 sampling traces) for high heating powers up to 4.5mW. The blue curve is in heating process while the yellow curve is in cooling process.

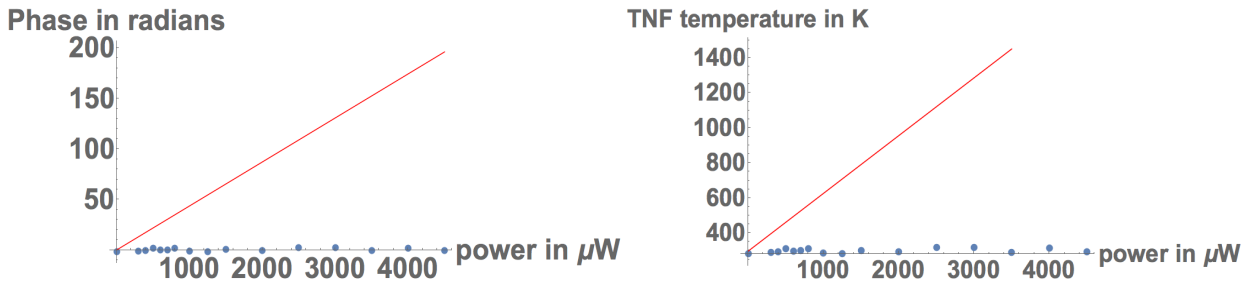

Figure 2.13: (left) Measured phase shift is plotted corresponding to the heating power from 0 to 4.5mW with the red line the expected change in phase; (right) Calculated TNF temperature from the measured phase shift as varying the heating power from 0 to 4.5mW with the red line the theoretical expectation

change of the fiber radius a[11]. This is equivalent to changing the effective refractive index of the fundamental mode guided through the TNF via the propagation constant $n_{\text{eff}} = \beta(V)/k_0$. Since we were only using hydrogen for this fiber pulling at that moment, a high flow rate was necessary to reach the critical temperature for softening the silica ($\sim$1450K). This gives the TNF a high pressure pushing it up during pulling and leads to a big arc bending upward close to the end of pulling so the TNF has to be pre-strained before fixing it to the bracket, which leads to an elongation of the nanofiber waist. We have not calibrated this elongation yet but it is reasonable to assume that this elongation ($\sim$2mm) is much larger than the axial thermal expansion of the nanofiber ($\sim \mu$m according to [11]). As a result, the axial thermal expansion of the TNF does not modify the length but only lowers its tensile stress.

$$\frac{\partial n(T)}{\partial T} = 9.627(9)\cdot 10^{-6} + 7.74(1)\cdot 10^{-9}(T - 299K) \tag{2.15}$$

$$\delta\phi = \frac{2\pi l_{\text{TNF}}}{\lambda}[n(T) - n(T_0)] \tag{2.16}$$

The temperature dependent thermo-optic coefficient is given by Eq. (2.15). This is an empirical formula obtained in reference [11] through fitting their experimental data for silica fiber over temperature range between room temperature up to around $1850K$. It describes how the refractive index of silica changes with its temperature (A wide range of characterization has been done in

literature.). The relationship between the temperature dependent refractive index and the phase measured in our experiment is given in Eq. (2.16), in which we take T_0 the room temperature 296K. In Fig. 2.13, on the left, I plot the measured phase shift corresponding to the heating power from 0 to 4.5mW and the red line shows the theoretical expectation; On the right, I plot the calculated TNF temperature from the measured phase shift as varying the heating power from 0 to 4.5mW compared to the theoretical expectation shown in red line.

The red line in Fig.2.13 shows the expectation of the relationship between the TNF temperature and the heating power: Without heating, we assume that the TNF stays at the room temperature 296K; As the heating power reached around 4.0mW, we observed an obvious deformation of the TNF through CCD camera, which indicated that the temperature of the fiber was close to the silica softening temperature. However, our experimental data processing shows inconsistency with this prediction. The temperature calculated from measuring the phase shift increases slowly with the increasing optical power and the highest temperature obtained at 320K is far below the softening temperature. We analyzed and concluded that the main reason for this inconsistency could be the dusts on the fiber. Reference [11] shows that 400mW heats their TNF to around 2000K for a fiber being produced in a clean room (no dusts on it at all). As shown in Fig. 2.8, our fiber is contaminated by randomly distributed dusts so that the heating along the fiber happens nonuniformly. This makes the experiment inconclusive because a local dust could heat the fiber to a much higher temperature than the other cold parts but the global phase we measured will not express this information. Moreover, a significant local heating source could generate a large radial thermal expansion at that point, which is difficult to analyze but make our model invalid. As a result, the temperature we calculated from this global phase is much lower than the expected temperature predicted from heating a clean fiber uniformly.

From Fig. 2.11 and 2.12, we can also see that the average phase differences from low power to high power do not vary significantly, which indicates that the SNR in this experiment might be still too low to extract significant information. One of the noise sources is that the heating laser

coupled into the TNF is transmitted through a long single mode polarization maintained patch cable connecting two optical tables. The specific winding geometry of this patch cable affects the matching between the polarization of the laser and the fiber axis, which results in a power fluctuation between $10 \sim 20\%$ for each heating power. Finally, any mechanical vibration occurring during the experiment also contributed to noise. We are making some improvements to the fiber pulling rig and perhaps this experiment can be repeated with a higher precision after a cleaner fiber is available.

Chapter 3

Experimental investigation on light-atom interaction using magneto-optical trap and tapered nanofiber

The first part of this chapter gives the basic theory for Magneto-optical trap (MOT). The second section describes the corresponding MOT setup in our lab. The third part includes the experiments we performed using MOT and TNF as well as the results. The last part analyzes the MOT temperature and calculates our dipole trap parameters.

3.1 A Rb magneto-optical trap

3.1.1 Velocity and position-dependent forces

The principle of operating a MOT relies on two forces: A velocity-dependent force that cools the atoms and a position-dependent force that traps them. The theoretical details can be found in different textbooks, for example, [12] and [13]. In **optical molasses**, three orthogonal pairs of counter-propagating laser beams are used to damp the atomic motion. In this process, the atoms are slowed down from momentum kicks with the red-detuned counter-propagating photons. The spontaneously emitted photons have random directions so they do not contribute to any acceleration or deceleration averagely ($\bar{F}_{\text{spont}} = 0$). During each momentum kick, the atom is going through a random walk, which is a slow diffusive movement. This type of scattering force, from the microscopic point of view, due to the inelastic collisions between photons and atoms, is proportional to the atomic scattering rate R_{scatt}, as shown in Eq. (3.1), in which Γ is the spontaneous decay rate of a single atom and ρ_{ee} is the atomic population in the excited state considering a two-level system in a steady state. Ω is the Rabi frequency and $\Delta = \omega - \omega_0 - \vec{k}\cdot\vec{v}$ is the detuning of the photons seen by the atoms. While from the macroscopic point of view, the optical molasses force is proportional

to the atomic velocity through a damping coefficient α, as shown in Eq. (3.2). Here I is the beam's intensity and I_{sat} is the saturated intensity for a two-level atomic system. The Rabi frequency and saturation intensity are related by $I/I_{\text{sat}} = 2\Omega^2/\Gamma^2$. Notice that α has to be positive to keep the molasses force a damping force, which requires the field to be red-detuned. The derivation from Eq. (3.1) to Eq. (3.2) can be found in reference [12].

$$F_{\text{cooling}} = \hbar k R_{\text{scatt}} = \hbar k \Gamma \rho_{ee} = \frac{\hbar k \Gamma \Omega^2}{4\Delta^2 + \Gamma^2 + 2\Omega^2} \tag{3.1}$$

$$F_{\text{cooling}} = -\alpha(\Gamma, \Delta, \Omega) \cdot \vec{v}, \text{ where } \alpha = 4\hbar k^2 \frac{I}{I_{\text{sat}}} \frac{-2\Delta/\Gamma}{[1 + (2\Delta/\Gamma)^2]^2} \tag{3.2}$$

$$T_D = \frac{\hbar \Gamma}{2k_B} \tag{3.3}$$

On the other hand, except for cooling, the atoms continuously illuminated by the near-resonant field will also go through heating. This is because of the random walks along the beam directions due to the spontaneous emission which acts as a fluctuating force. Random recoils cause the mean square velocity to increase and finally the competition between the cooling and heating processes leads to a stationary state, which determines the so-called **Doppler cooling limit**, given by Eq. (3.3). It gives the lowest temperature expected in the optical molasses technique. It happens when $\Delta = -\Gamma/2$ as Ω approaching zero. For ^{87}Rb D_2 line, $\Gamma = 38.117$MHz, so $T_D \approx 146\mu$K. Considering the specific power of the cooling beam, the specific value for the lowest temperature that could be reached in the experiment can be calculated (see section 3.4).

Even though atoms can be cooled at the intersection region, this is not a trap. The atoms can still wander away from the center and experience no force pulling them back. They are allowed to diffuse freely and even escape. In order to obtain a restoring force that traps the atoms an inhomogeneous magnetic field is used. The quadrupole magnetic field $\vec{B}(x,y,z)$ vanishes at the center of the trap and increases linearly in all directions. The $\vec{B}(x,y,z)$ shifts the atomic energy Zeeman sub-levels by an amount proportional to the distance of the atoms away from the center

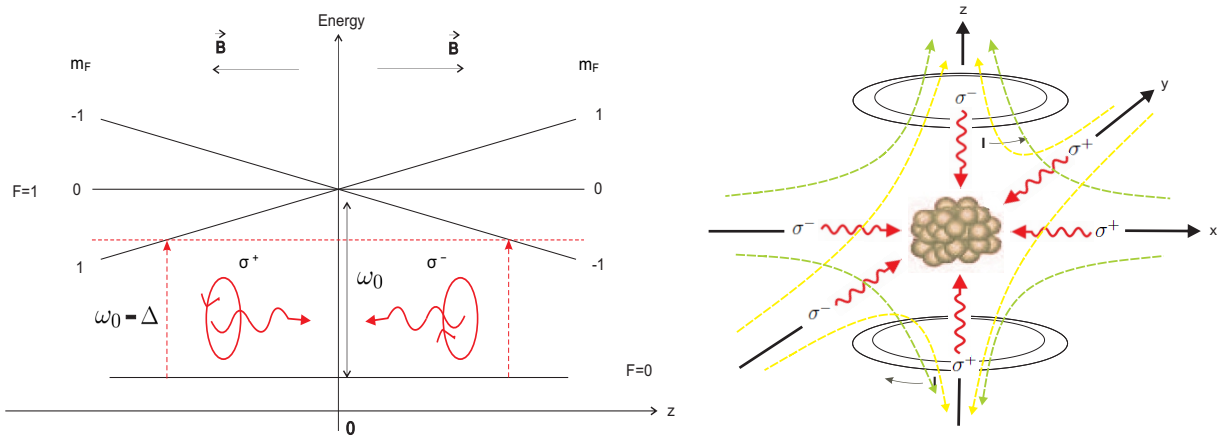

Figure 3.1: (left) The principle of MOT illustrated for the simplest case of an atom with F=0 to F=1 transition; (right) Three-dimensional mechanism of MOT

of the trapping $\Delta E(x,y,z) = g\mu_B m_F B(x,y,z) = g\mu_B m_F b \times z$, in which μ_B is the Bohr magneton and m_F is the Zeeman sub-level value of the atoms. $g = g_{F'} M_{F'} - g_F M_F$ is in general for a transition between the hyperfine structure levels $|F, m_F>$ and $|F', m_{F'}>$.

Fig. 3.1 (left) demonstrates the principle of MOT for the simplest one-dimensional case between ground state level $F = 0$ and excited state level $F' = 1$. Two beams of red-detuned, counter-propagating and orthogonal in polarizations are necessary. The σ^- couples the $\Delta m_F = -1$ transition and the σ^+ couples the $\Delta m_F = +1$ transition, generating restoring forces on atoms pointing to the trapping center. The generalization of this simple 1D example to 3D is straightforward. In Fig. 3.1 (right), three pairs of counter-propagating, red-detuned laser beams together with the field $\vec{B}(x,y,z)$ created by two coils in anti-Helmoltz configuration trap and cool the atoms at the intersection area of the beams and the zero point of the $\vec{B}$ field. In summary, a force shown as Eq. (3.4)[12], is working on the atoms to form an atomic cloud at the center of the alignment. Here, $\alpha\beta/k$ is the spring constant in the restoring force, in which k is the wavevector and $\beta z = \frac{g\mu_B}{\hbar}\frac{dB}{dz}z$.

$$F_{\text{MOT}} = -\alpha v - \frac{\alpha\beta}{k} z \tag{3.4}$$

3.1.2 Atomic transitions and laser system

We are using ^{87}Rb D_2 Line for our laser cooling and trapping. The cooling laser is roughly resonant without locking on the transition of $5^2S_{1/2}\ F = 1 \rightarrow 5^2P_{3/2}\ F' = 2$ ($\lambda \approx 780.232$nm). Each cooling beam has an intensity of around 0.31mW/cm^2 in maximum. The trapping laser is red-detuned around 14.6MHz from the closed-cycle transition of $5^2S_{1/2}\ F = 2 \rightarrow 5^2P_{3/2}\ F' = 3$ ($\lambda \approx 780.246$nm). Each trapping beam has an intensity of around 5.70mW/cm^2 to 8.15mW/cm^2 depending on the alignment and fiber coupling efficiency. The transitions are shown in Fig. 3.2 and the corresponding atomic absorption spectroscopies are shown in Fig. 3.3 with some extra information on D_2 transition is given in Table 3.1.

Fig. 3.3 (left) shows how the atomic saturated spectroscopy looks like from our trapping laser on the oscilloscope. Basically, there is a beam of tens of μW double passing through a Rb vapor cell and being detected by a photodetector. The picture here shows the electronic signal directly from the photodetector that converts the optical signal proportionally. We are scanning the laser frequency over time so that when it is on resonant with a specific atomic transition, there is a dip appearing in the transmitted power. The two big dips are Doppler-broadened absorption lines corresponding to ^{85}Rb ($F = 3$) and ^{87}Rb ($F = 2$) transitions with a typical linewidth $\sim$500MHz. The small peaks sitting on the big dips are saturated absorption spectrum, which results from the increased transmission of the second passing beam due to the first passing beam saturating the atoms in the cell. Since these two beams are counter-propagating, saturated absorption spectrum probes the special group of atoms that have zero velocity. The cross-over saturated spectrum is also shown in the picture, e.g., F' =2 x 3. This spectrum probes the special group of atoms that have the velocity which allows them to absorb the red-detuned photons coming towards them and the blue-detuned photons running after them. As a result, this equal possibility will reduce the absorption of one of the beams and generate a peak on the transmission line which corresponds to the middle frequency between two hyperfine levels.

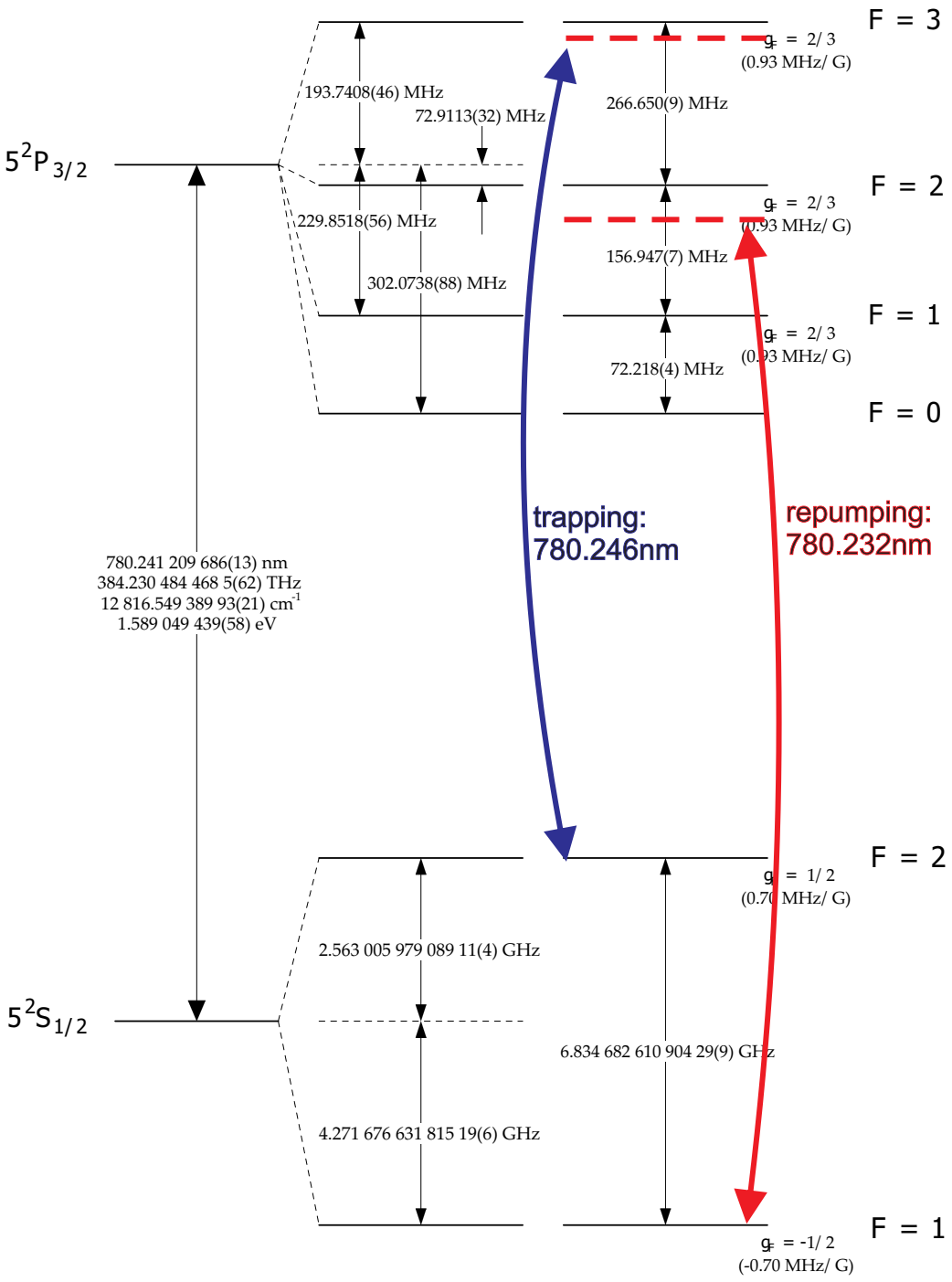

Figure 3.2: ^{87}Rb D_2 Line transitions [14] with marked cooling and trapping transitions

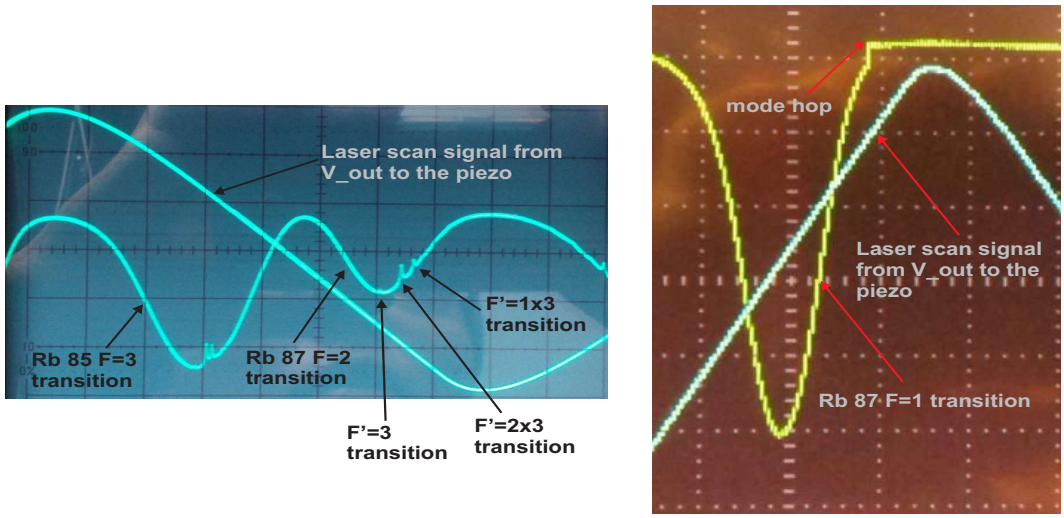

Figure 3.3: (left) Saturated atomic absorption spectroscopy of trapping laser and (right) Doppler broadened spectroscopy of cooling laser from our home-made ECDLs

Parameters	**Symbol**	**Values**
D_2 Decay Rate / Natural linewidth	Γ	$2\pi \times 6.065(9)$ MHz
D_2 Lifetime	$\tau = 1/\Gamma$	26.24(4) ns
D_2 Doppler cooling limit temperature	T_D	146μK
Dipole moment ($\sigma^{\pm}$ - polarized light)	$d_{(m_F=\pm 2 \rightarrow m_{F'}=\pm 3)}$	$2.534(3) \times 10^{-29}$ C·m
Resonant Cross Section ($\sigma^{\pm}$ - polarized light)	$\sigma_{0(m_F=\pm 2 \rightarrow m_{F'}=\pm 3)}$	$2.907 \times 10^{-9} cm^2$
Saturation Intensity ($\sigma^{\pm}$ - polarized light)	$I_{sat(m_F=\pm 2 \rightarrow m_{F'}=\pm 3)}$	1.669(2) mW/cm^2

Table 3.1: Some parameters of ^{87}Rb D_2 transition

3.1.3 Vacuum system and Rb source

In our system, an octagonal stainless steel chamber with 8 small view ports, 4 of which are used as windows for the MOT beams. One port is used for atomic source, one port is used for fiber feedthrough, one port is connected to UHV pumps and the last one, facing down, is not used (ref to Fig. 3.4). The typical pressure shown from the ion pump gauge is between 2×10^{-9} and 4×10^{-8} torr. The valve shown in Fig. 3.4 is used to isolate the UHV system from the mechanical and turbo pumps as the pressure is below 10^{-7} torr then we only use the ion pumps to maintain the UHV.

Atomic source is Rb dispenser, RB/NF/3.4/12 FT10+10, from SAES. We normally operate 4 dispensers at the same time in a series configuration and feed a current between 5A and 9A, depending on the running time. This type of dispenser has Rb of 3.4mg/each and a very small percentage of Rb getter so it is normal to observe a pressure improvement after turning off the current. Some bakeout and degassing were done at the very beginning [6] and bakeout is recommended every time after breaking the vacuum system.

3.1.4 Magnetic coils and polarization preparation

Magnetic field Our workshop-made copper coils have $N = 400$ turns and radius $R = 7.6$cm, being $2A = 8$cm apart from each other. The resistance of putting them in series is 10Ω and we usually operate them with a current of $I_0 = 2$A. The $\vec{B}$ field can be calculated according to Eq. (3.5), in which $K(k^2)$ and $E(k^2)$ are the first and second kinds of the incomplete elliptic integral. Since we are only interested in $\vec{B}(z)$, we take $\rho = 0$ in our calculation and Fig. 3.6 shows our $\vec{B}(z)$ due to each coil and the total field due to two coils. The gradient close to the center is around 10G/cm.

$$B(z) = \frac{\mu_0 I_0 N}{2\pi} \frac{1}{\sqrt{(R+\rho)^2 + (z-A)^2}} [K(k^2) + \frac{R^2 - \rho^2 - (z-A)^2}{(R-\rho)^2 + (z-A)^2} E(k^2)] \tag{3.5}$$

Polarization preparation Our cooling and trapping beams are combined using an evanescent coupling fiber beam splitter and sent into chamber through six optical "cages" (Fig.3.4). The polarization generation and inspection are shown in Fig.3.7, in which lens 1 is used to collimate

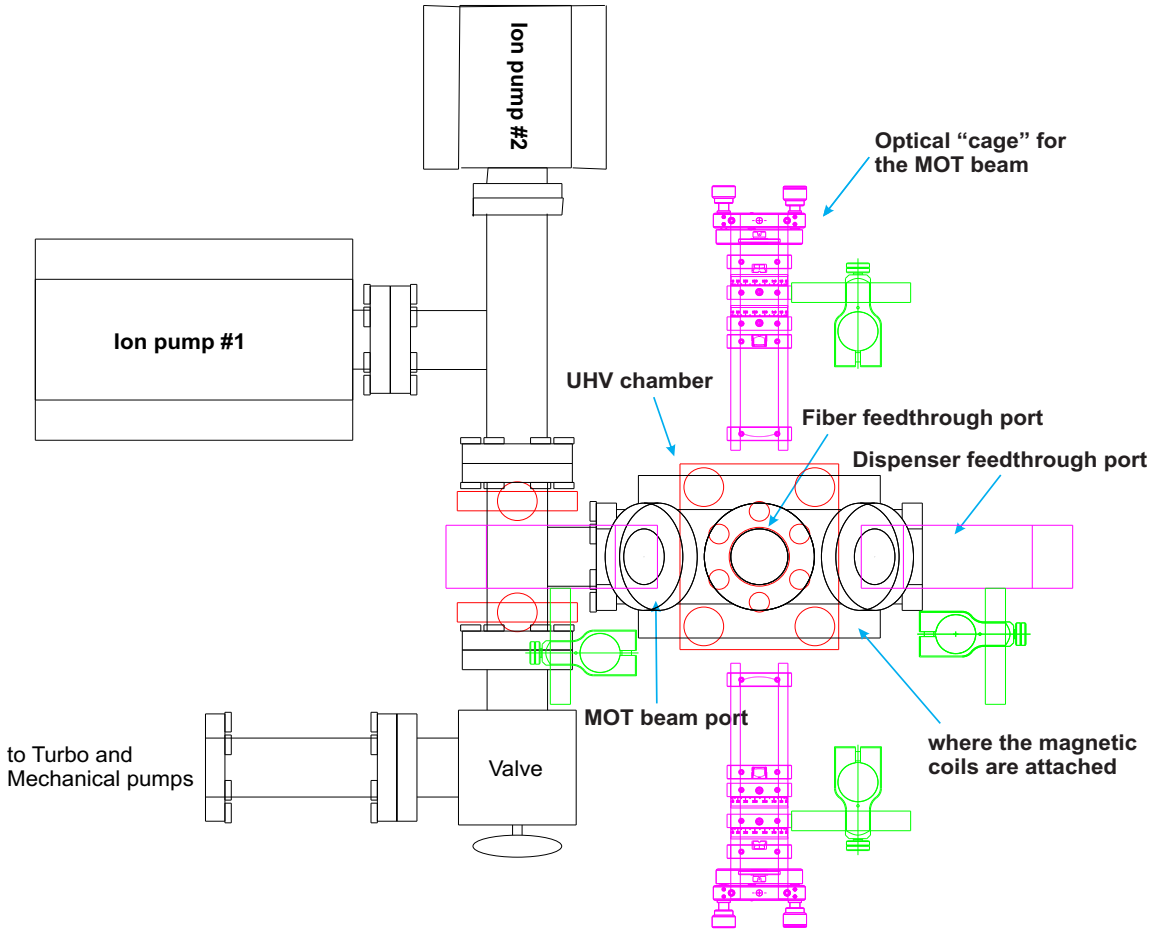

Figure 3.4: Vacuum chamber configuration (top view)

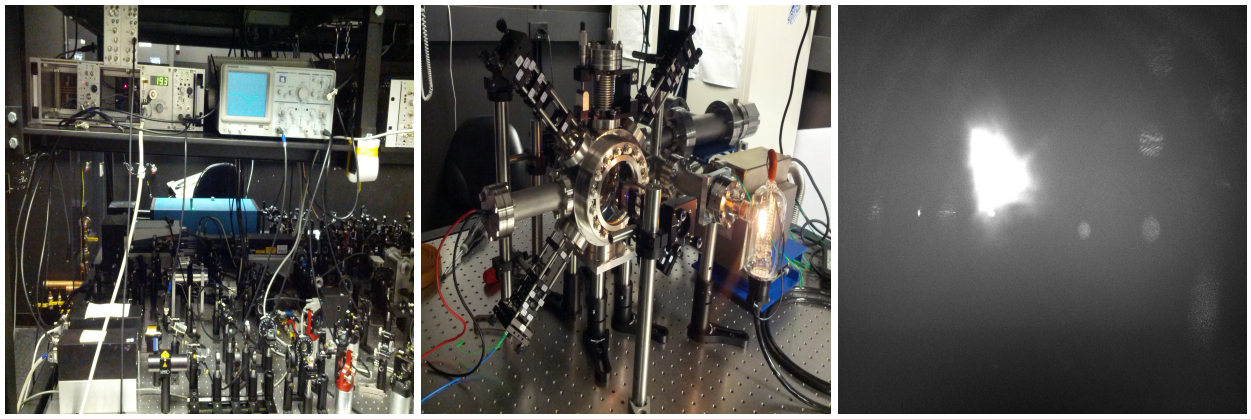

Figure 3.5: Pictures of our optical setup (left), UHV chamber (middle) and MOT (right)

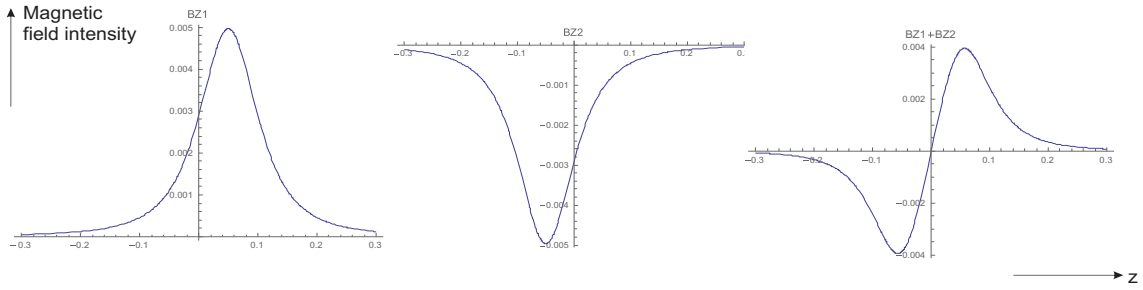

Figure 3.6: $\vec{B}(z)$ calculation: $\vec{B}_1(z)$, $\vec{B}_2(z)$ due to single coils (left and middle) and the total $\vec{B}(z)$ (right)

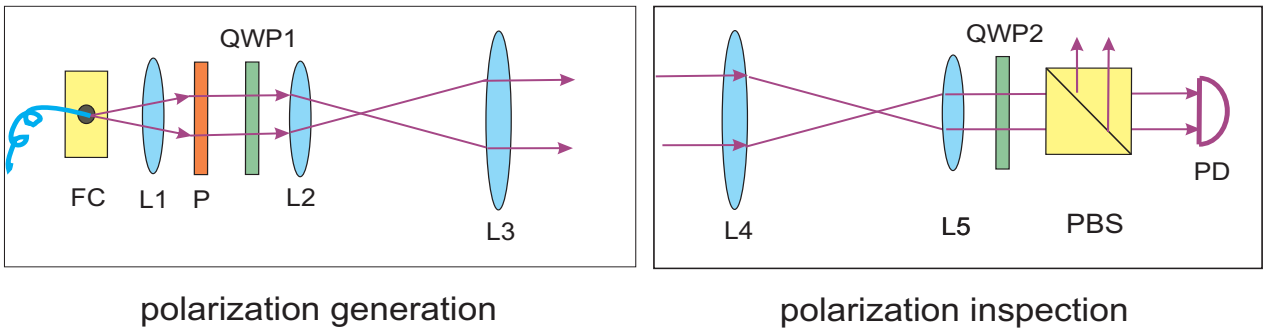

Figure 3.7: Polarization preparation and inspection of the optical "cages" for MOT

the beam coming out from the single mode fiber (SMF) and the polarizer after allows to balance the power of the six beams. The quarter wave plate (QWP) with an angle of 45° or −45° with respect to the polarizer determines the polarization to be σ^+ or σ^-, after which there is a telescope formed by lens 2 and 3 to expand the beam to 2.5cm in diameter. The inspection follows the same logic: telescope of lens 4 and 5 makes a smaller beam then a QWP changes σ^+ or σ^- back to $|H\rangle$ or $|V\rangle$ followed by a photodetector(PD). Given the logic that **first**, the polarization is defined with respect to the wave vector direction and **second**, $(\vec{\bigtriangledown}\cdot\vec{B})_z = -2(\vec{\bigtriangledown}\cdot\vec{B})_x = -2(\vec{\bigtriangledown}\cdot\vec{B})_y$, the polarizations have to be prepared in such a way that the four beams in the chamber plane have the same polarization (All of them have maximum transmission/reflection at the PD in the inspection.) and the other two beams along the $\vec{B}_z$ axis have the opposite polarization (They have maximum reflection/transmission at the PD in the inspection.)

Once the polarization of the input beam in front of the fiber coupler is fixed and aligned with

the polarization-maintained fiber (PMF) axis (This can be done through using a HWP before the fiber coupler and rotating it while monitoring the fiber transmission until it reaches the maximum value since the PMF has the lowest loss when the beam polarization is maintained.), and the angles between P and QWP in the "cages" are found and fixed to produce circular-polarized beams, the fibers and cages should not be disturbed anymore. However, mechanical instability happens with time and powers need to be balanced using the polarizers thus the QWPs also need to be rotated accordingly by the same angle to keep the polarizations the same. If it is difficult to form a reasonable MOT and all the other factors have been excluded, the "cages" need to be taken down for polarization check since the angles between P and QWP might change (This happens every few months.).

3.2 Description of the experimental setup

3.2.1 A general experimental schematic

The full experimental layout with local modifications for different experiments is shown in Fig, 3.8. The light orange part includes spectroscopies for both cooling and trapping lasers, two AOMs (model number 1205C-x Isomet) used to generate side bands for experimental switches and frequency detuning, a tapered amplifier (TA, similar to model number EYP-TPA-0780-01000-3006-CMT03-0000) for the trapping laser to amplify the side band power from the AOM for by 90-100 times depending on the input power. The cylindrical lens and telescope after the TA form a mode-cleaning mechanism to improve the mode matching to the fiber coupler, which usually has a coupling efficiency of 50-60%. The fluorescence from TA itself is around 45-50mW depending on the feeding current ($\sim$2A) and a good alignment to the TA could guarantee a good fiber coupling if nothing changes in between.

The light green part is where the MOT and TNF are brought together. Cooling and trapping beams are coupled separately and combined through a 2 to 6 fiber beam splitter, which modifies the final polarizations all along the PMF axis and sends the beams to six optical "cages". Two

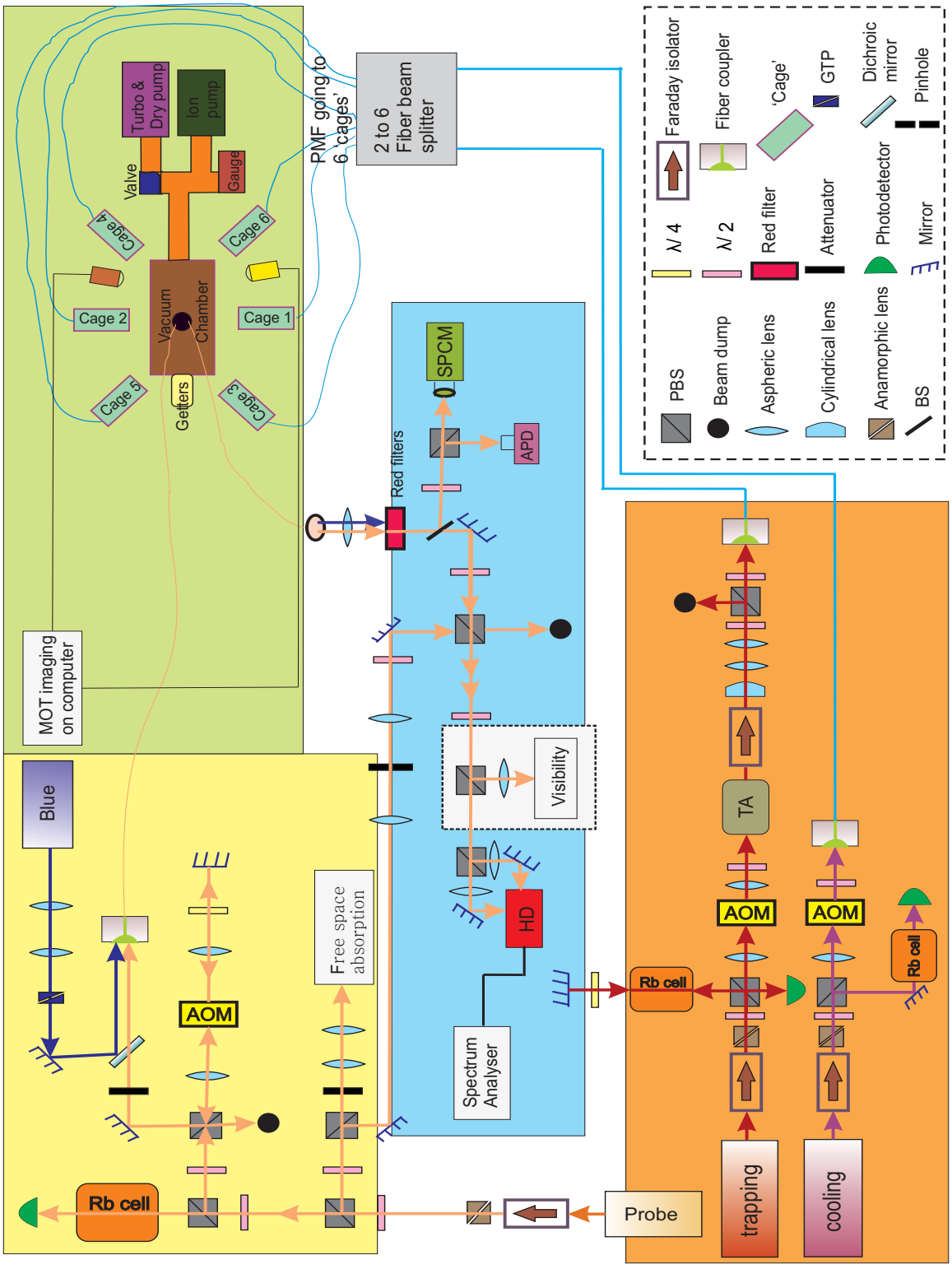

Figure 3.8: A general experimental schematic

CCD cameras are used to check the overlap of the MOT and TNF from two orthogonal angles.

The light yellow part is the preparation of the experimental beams. There is a probe laser that is used for multiple purposes. One of them is to investigate the MOT through free space absorption. It is on resonance with ^{87}Rb D_2 Line with some flexibility of being locked onto different transitions for different experiments. An AOM switch is also used to detune as well as scan the laser frequency under the control of a Voltage-controlled oscillator (VCO). The probe laser's power is split into four parts: spectroscopy, Local Oscillator (LO) in homodyne/heterodyne detection, free-space absorption and double-passing the AOM for TNF launching, with HWP+PBS combination in each way to adjust the power. There is also a blue laser used initially to help avoid atoms falling onto the TNF through offering a repulsive dipole force but we stop using it after a while since we found that the red laser would help the TNF desorb the atoms through heating it up quite effectively.

The light blue part shows some experiments that are slightly different for each local measurement. On one side, we can use single photon counting module (SPCM) or avalanche photodiode (APD) depending on the requirements of the experiments. On the other side, we can do homodyne/heterodyne detection, which will be described in detail in the following sections.

3.2.2 MOT switches and the timing series

In atomic physics experiments, switches on MOT beams and on experimental beams are very popular to use to avoid saturating the atoms as well as to control the measurements. Optical switches are realized through AOMs and we have a home-made switch to control the $\vec{B}$ field. To synchronize all the switches, a pulse generator (BNC 565) is used as the central clock with adjustable TTL width and delay, whose signals are sent to externally modulate the signal generators that control the AOMs.

The MOT beams and the $\vec{B}$ field have the opposite timing series with the probe beam, as shown in Fig. 3.9. The probe beam is off when the MOT is reformed to avoid affecting the trapping forces while the MOT beams are off when the probe beam is on to avoid affecting the absorption from the weaker probe beam. The frequency scan of the probe beam when it is on is realized through

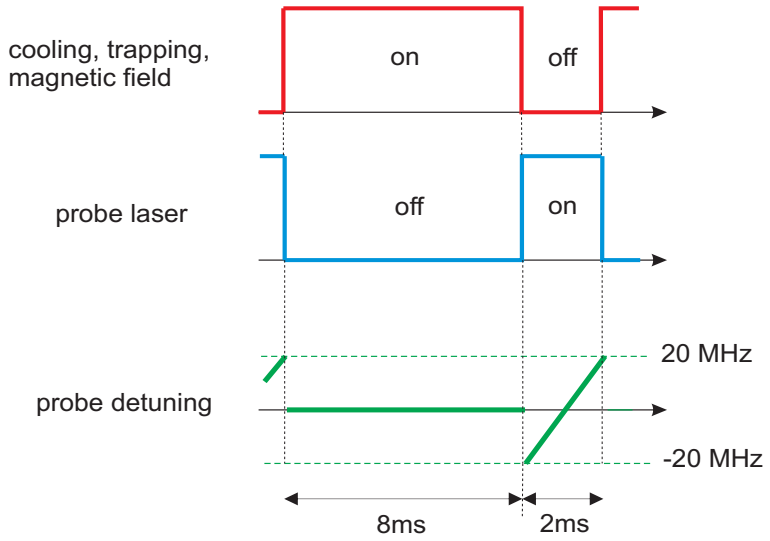

Figure 3.9: Timing sequence used in the experiments to switch on/off the MOT beams and $\vec{B}$ field while scanning the probe laser

the VCO, whose RF output to the AOM is linearly related to the input voltage (ramp signal). Considering the bandwidth of the AOM, 60MHz to 90MHz, a 5-10V ramp signal is used to drive the VCO, which generates an RF signal that sweeps the AOM between 126MHz and 166MHz after a double pass. Thus, the probe beam is scanning over 40MHz, which could be manually tuned to cross over the atomic transitions and cover the absorption linewidth of 6MHz of cold atoms. The ON and OFF parts do not have to be fixed at 8ms and 2ms. It depends on specific situations. For example, the lower limit of the probe laser pulse duration should be the bandwidth of the APD/SPCM and the upper limit should be the time-of-flight of atoms released from the MOT. Switching off the $\vec{B}$ field helps avoid the inhomogeneous broadening (due to Zeeman splitting) of the measured absorbance profiles of the cold atoms (the broadening is $\sim$ 1MHz in [3]).

The circuit for the $\vec{B}$ field switch is shown in Fig. 3.10 (above). The purpose of this switch is to turn on and off the magnetic field during experiment as fast as a few ms. Having the $\vec{B}$ field back is to retrap the atoms and turning off the $\vec{B}$ field is to avoid the Zeeman broadening. It is the version from [15] with modifications in red. Keep in mind the rules for a transistor to be ON: $V_c > V_e$ by at least a few $\times$ 0.1 V; $V_b > V_e$, usually $V_b = V_e + 0.6$ V; $V_c > V_b$ and when it is ON, $I_e = (\beta + 1)I_b$

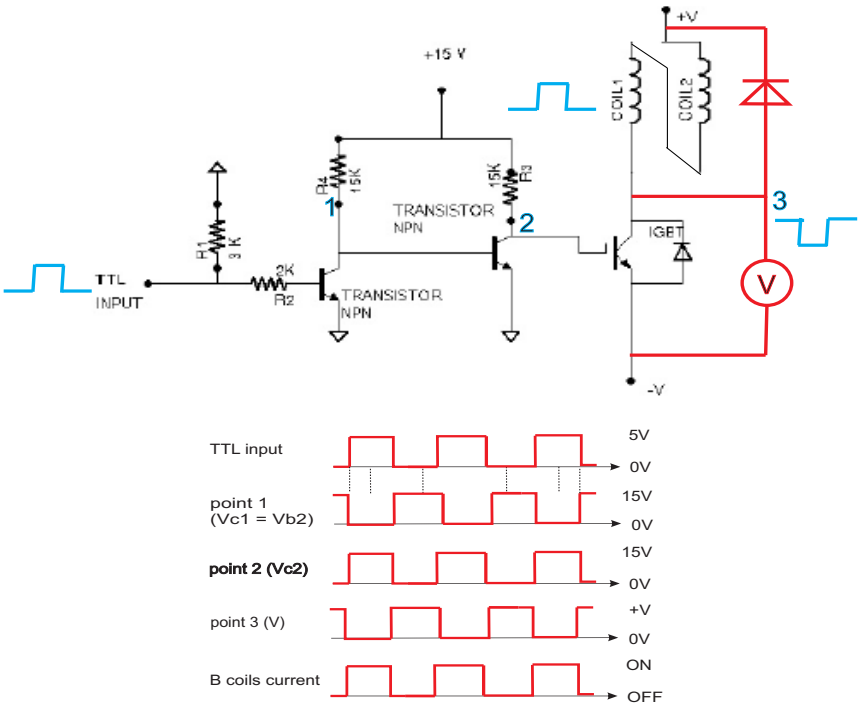

Figure 3.10: (above) Circuit schematic for $\vec{B}$ field on/off switch [15]; (below) Corresponding schematic analysis

$\approx I_c$. Thus it is straightforward to analyze the circuit as shown in Fig. 3.10 (below). The "clamD diode" is used to eliminate the spike-like kicks happening at the edges of the on/off switch (It is possibly due to the eddy current of the magnetic coils because we did not observe the same kicks with resistors.) and the voltmeter is placed to monitor the signals.

3.3 Some experiments and the results

3.3.1 Free-space absorption and MOT characterization

Before attempting atomic absorption through TNF we first probe the MOT with a free-space propagating weak beam and the MOT size, number of atoms in MOT, MOT density and a rough MOT time-of-flight (the $1/e$-decay time of the atomic density after the MOT mechanism is off) are determined. As mentioned above, the probe laser is tuned to the trapping laser frequency so that aligning it to the MOT and seeing disturbance would be easier. There is a telescope to adjust the

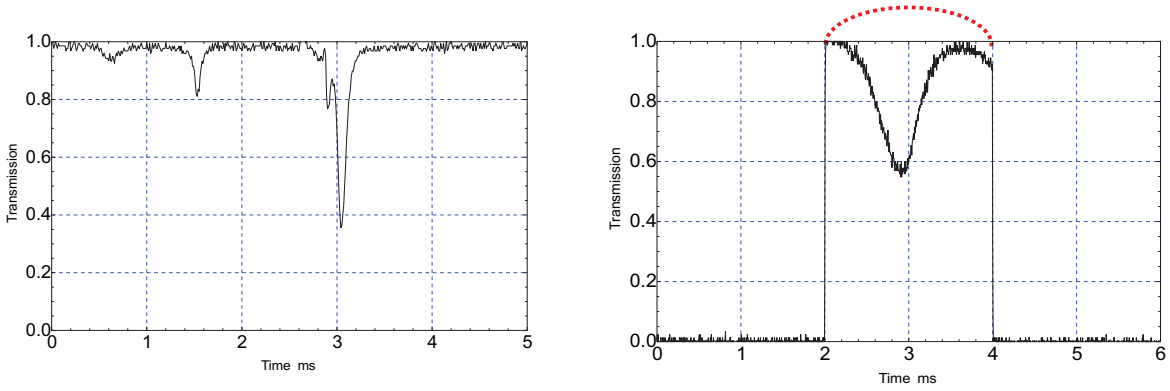

Figure 3.11: (left) Free space absorption **without** switching on/off the MOT mechanism, the laser was scanning over ∼200MHz between 0-5s; (right) Free space absorption **with** switching on/off the MOT mechanism, the laser was scanning over 40MHz between 2-4s

probe beam width and we observed that the MOT completely disappeared at a beam width ∼3mm (which we roughly take as our MOT size). A precise measurement could be analyzing the Gaussian profiles from either the CCD images of the MOT or the TNF scanning absorption along the MOT.

A 8μW probe beam passes through the MOT and is focused onto a photodetector. Without switching on/off the MOT mechanism, the absorption we observed is 60%∼75% (O.D. is 1.0∼1.34 according to the definition O.D.$\equiv -\ln\frac{P_{\text{out}}}{P_{\text{in}}}$), while an absorption of ∼40% with switching was observed, as shown in Fig. 3.11. Without switching, the peak absorption depends on the spacial area the probe beam probes the MOT. With switching, the duty cycle of pulses that determines the MOT loading time and the time-of-flight of the MOT also matters. The absorption linewidth for ^{87}Rb is ∼6MHz due to the elimination of inhomogeneous broadening from cold atoms and the homogeneous broadening of the Lorentz profile from a single atom.

Without switching Given a power of 8μW with a beam radius around 1.5mm, the probe beam has an intensity ∼0.11 mW/cm^2, which is much less than the saturation intensity I_{sat} (see Table 3.2) and so has negligible mechanical effect on the atomic cloud. Each trapping beam has a power around 30mW, considering the $r_{\text{cooling}} = 1.25$cm, the intensity of the trapping beams is 36.7mW/cm^2, which is much higher than I_{sat}. Thus we can assume that $\rho_{gg} = \rho_{ee} \approx 0.5$, which

Speed of Light	c	2.997 924 58$\times 10^8$ m/s (exact)
Permittivity of Vacuum	ε_0	8.854 187 817 ... $\times 10^{-12}$F/m
Planck's Constant	$\hbar$	1.054 571 628(53)$\times 10^{-34}$ J·s
Decay Rate/Natural Line Width (FWHM)	Γ	38.117(11)$\times 10^6$ s^{-1}
Dipole Moment $\|F=2,m_F=\pm 2>\rightarrow\|F'=3,m'_F=\pm 3>$, cycling transition ($\sigma^{\pm}$-polarized light)	d	2.534 44(52)$\times 10^{-29}$ $C{\cdot}m$
Saturation Intensity, $\|F=2,m_F=\pm 2>\rightarrow\|F'=3,m'_F=\pm 3>$, cycling transition ($\sigma^{\pm}$-polarized light)	I_{sat}	1.669 33(35) mW/cm^2
Resonant Cross Section, $\|F=2,m_F=\pm 2>\rightarrow\|F'=3,m'_F=\pm 3>$, cycling transition ($\sigma^{\pm}$-polarized light)	σ_0	2.906 692 937 721(66)$\times 10^{-9}$cm^2

Table 3.2: Basic parameters used in the calculation for MOT characterization[14]

can be proved through calculation. Given that the trapping laser detuning $\Delta_{\text{cooling}} = 9$MHz, the trapping laser power P_{total}=180mW(30×6) and the field magnitude $|\vec{E}| = \sqrt{\frac{P_{\text{total}}}{c\varepsilon_0\pi r^2_{\text{cooling}}}}$, the Rabi frequency can be calculated $\Omega = d \times |\vec{E}|/\hbar \approx 89.7$MHz (parameters see Table 3.2). The weak probe beam has to compete with the cooling beam as far as absorption of light by the atoms is concerned since only those atoms staying in the ground state will absorb the probe energy. Using the above results in Eq. (3.1), we have $\rho_{gg} = 1-\rho_{ee} = 1-\frac{\Omega^2}{\Delta^2_{\text{cooling}}+\frac{\Gamma^2}{4}+2\Omega^2} \approx 0.51$. Now we can estimate the number of atoms in the MOT as well as its density.

Beer-Lambert law, shown in Eq. (3.6), describes how the absorption relates to the medium properties, in which $\frac{I_{\text{out}}}{I_{\text{in}}} = \frac{P_{\text{out}}}{P_{\text{in}}}$, σ_0 is the single atom resonant cross/scattering section, n is the atomic density, l is the length of the medium interacting with the light, N_{gg} is the number of atoms in the ground state and A is the probe laser beam cross section. The second equality is true only when the probe beam width just covers the whole MOT, which is roughly the case in our experiment.

$$\frac{I_{\text{out}}}{I_{\text{in}}} = \exp(-\sigma_0 nl) = \exp(-\sigma_0\frac{N_{gg}}{A}) \tag{3.6}$$

Taking 25% transmission, 1.5mm beam radius, we have $N_{gg} \approx 3.4\times 10^7$ so the total number of

atoms in the MOT is $N = N_{gg}/\rho_{gg} \approx 6.6 \times 10^7$. Thus the density of our atomic cloud is estimated to be $\rho_{\mathrm{MOT}} \approx 4.6 \times 10^9/\mathrm{cm}^3$. These values are well within the expected range for a standard MOT.

With switching To avoid the competition of the probe laser with the trapping laser and to have more atoms in the ground state, the MOT mechanism is switched on/off with a timing sequence shown in Fig. 3.9. The reason for choosing this 80% duty cycle was explained in section 3.2.2. Since we have a metal chamber, it is also important to switch on/off the $\vec{B}$ field less faster than the duration of the eddy current, which is around 2ms by experience. The 8ms was chosen because we observed an optimal absorption with the MOT reloading time. The scanning of the probe laser as well as the design and implementation of this switch were discussed in section 3.2.2. The absorption signal becomes quite weak after turning off the MOT mechanism for more than 3ms, which indicates that the MOT lifetime would not be longer than this value. There are a few factors that affect the MOT lifetime, i.e., MOT expansion affected by its temperature and gravity, the base pressure (Our UHV system has a pressure gradually oscillating between 5×10^{-9} and 2.5×10^{-8} torr.). Thus the MOT lifetime highly depends on specific experimental parameters and should be optimized each time while doing the experiments.

A reasonable expectation is to see a higher absorption through the probe beam from the MOT after switching off the MOT mechanism compared to having it on. It is because that switching off the MOT beams would increase the number of atoms in the ground state within the MOT lifetime, which would in turn increase the possibility of absorbing the probe beam photons. However, our results shown in Fig. 3.11 seem to be contradictive. We analyzed the possible reasons for this. First, in the absorption measured in the left figure, the laser is scanned fully by the laser scan controller with a frequency around 100Hz. In this case, the power of the probe laser is stably maintained at 30μW. In the absorption measured in the right figure, the laser frequency is scanned through an AOM which is controlled by a VCO. The central frequency of the AOM is 65MHz and we are scanning it from 55MHz to 75MHz. The power of the probe beam is varying, as indicated by the red dotted line in Fig. 3.11, according to the change in the scanning frequency with the

highest power at 65MHz. In this case, the absorption line shape with switching could be slightly affected; Second, the frequency of the probe laser was not locked at the atomic transition. Instead, in the experiment, we manually changed the voltage on the scanning piezo to search for the right resonant frequency. In this case, the laser frequency could move away from the atomic transition very fast, which will affect the absorption. The third possible reason is the time-of-flight of the MOT atoms. An empirical value for a base pressure of 10^{-8} torr is 1-2ms, which means that we almost lost all the atoms within half of the scanning time. Assuming that our MOT radius is around 1mm and the MOT temperature for a 9mW cooling laser is around 250μK, the average velocity of the atoms can be calculated to be around 0.15m/s. Thus it will take the atom at the center of the MOT around 6.7ms to be untrapped. For atoms not at the center, it will take much less time to get out of the trap. Moreover, after switching off the cooling beam, the atoms will become hotter and the time-of-flight could be even shorter. This makes us think that the switch might not be fast enough in this experiment to observe a high optical depth.

The attempt for atomic absorbance through TNF and the potential problems Three compensation coils are used to slightly move the MOT position along x, y and z directions (within 2mm) away from the chamber center. Two micrometric screws are used to move the TNF position around the center. Two CCD cameras are used in two orthogonal directions to allow the best overlapping of the MOT and TNF. As shown by the calculation in the next section, the effective number of atoms that interact with the evanescent field is $3 \sim 6$, so the probe laser power used for TNF evanescent field spectroscopy has to be low enough to avoid saturating the single atoms. If we assume that there are 4 atoms are in the ground state, the probe laser power needs to be as low as $P = \hbar\omega_0\Gamma N = hcN\Gamma/c$ =45pW. We are still developing a detection mechanism in our lab for such a low power measurement (Our APD could not detect optical power lower than 500pW and a further homodyne/heterodyne measurement did not give any beating signal at the pW level plus the electronic noise at frequency zero spanning makes the movement of a DC signal even more difficult to be observed.).

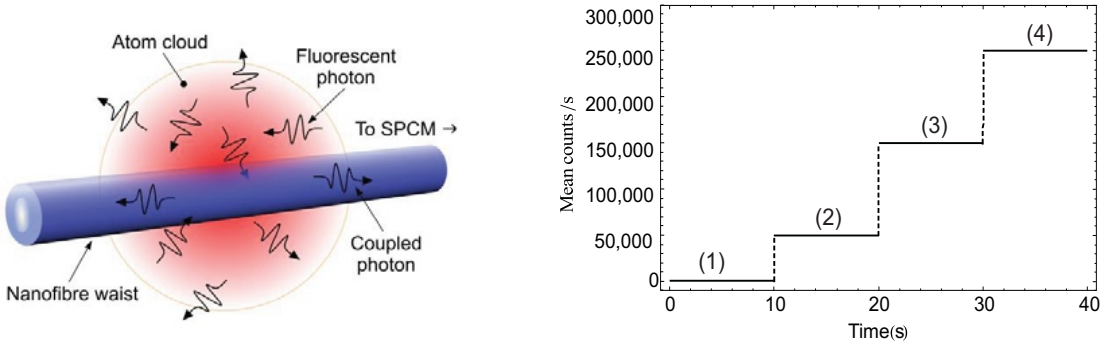

Figure 3.12: MOT fluorescence coupled into TNF detected by SPCM with experimental demonstration (left) and collected data (right)

Another potential problem is the real number of atoms that interact with the field in such a dynamic environment. Launching laser into the TNF will heat it up that will in turn heat up the atoms close to it so the effective number of atoms might be even lower[3]. Also it is technically challenging to move the densest part of the MOT so precisely to the thinnest part of the fiber. We are still putting more effort to improve the adjustability and precision of this whole system.

3.3.2 Probing the fluorescence of laser cooled atoms through TNF

The fluorescence from the MOT coupled into the TNF fundamental mode is measured using SPCM, which is free-space coupled to the output of the optical fiber, as shown in Fig. 3.8. The reason behind this configuration is that a 475nm blue laser is launched all the time through the TNF to help avoid atoms falling onto the fiber surface due to its repellent dipole force. Thus red filters are used at the fiber output to filter out this auxiliary wavelength. The observed photon counts are plotted in Fig. 3.12 for four different conditions: In the first 10s, the ambient room light plus dark counts give a mean number of counts around 1KHz; In the next 10s, the blue laser (power 10μW) is turned on and increases the counts to 50KHz; During the next 10s, the MOT beams are switched on and 150kHz is registered and for the last 10s, we turn on the $\vec{B}$ field and the MOT is formed and overlapped with TNF. A mean number of 250KHz counts is observed. Thus, we observe around 10^5 counts/s from the MOT fluorescence coupled into the guided mode in TNF.

The fluorescence photon count rate is related to other experimental parameters according to $n_p = N_{ee} R_{scat} \eta_{fiber} T_{fiber} \eta_D$ ([16]), in which N_{ee} is the effective number of atoms in the excited state around the TNF and R_{scat} the atomic scattering rate. η_{fiber} is the averaged coupling efficiency of the spontaneously emitted photons into the fiber guided mode. T_{fiber} is the fiber transmission from the mid-TNF to one end, which is the square root of the total transmission. $\eta_D \approx 50\%$ is the quantum efficiency of our SPCM (already optimistic for free-space coupling). In our experiment, the MOT beam intensity is close to saturation intensity so $\rho_{ee} \approx 0.5$, which gives the total photon scattering rate $R_{scat} = \Gamma \rho_{ee}(t \to \infty) = 38.1\text{MHz} \times 0.5 \approx 19.1\text{MHz}$. Our TNF, after pulling, has an average transmission around 94%. Considering two 0.1dB splicing loss on each end, the final transmission T_0 after being launched into the UHV system, is at most $94\% \times (97.7\%)^2 \approx 89.8\%$ ($10 log_{10} \frac{P_{\text{out}}}{P_{\text{in}}} = -0.1\text{dB}$, so $\frac{P_{\text{out}}}{P_{\text{in}}} \approx 0.977$). Thus $T_{fiber} = \sqrt{T_0} \approx 94.75\%$ and $n_p = 10^5$ counts/s. To estimate N_{ee}, given $a_{TNF} \approx 180\text{nm}$ and the red- and blue-detuned laser wavelengths we used to be 780.246nm (attractive) and 475nm (repelling), solving Eq. (2.1) for β gives $\beta_{\lambda=780.246\text{nm}} = 8.57\mu\text{m}^{-1}$ and $\beta_{\lambda=475\text{nm}} = 16.3\mu\text{m}^{-1}$. Calculating the decay lengths for both fields through $\Lambda = \frac{1}{q} = \frac{1}{\sqrt{\beta^2 - k_0^2 n_2^2}}$ ($k_0 = 8.05\mu\text{m}^{-1}$ and $n_2 = 1.0$) gives $\Lambda_{\lambda=780.246\text{nm}} \approx 342\text{nm}$ and $\Lambda_{\lambda=475\text{nm}} \approx 70\text{nm}$. To this end, we have an effective observation volume around the TNF of $(342 - 70)\text{nm} = 272\text{nm}$ thick hollow cylinder with roughly 1$\sim$2 mm length. Considering our MOT density ($\sim 4.6 \times 10^9 \text{atoms/cm}^3$), we have $N_{ee} = \rho_{\text{MOT}} \times \text{volume} \approx 3 \sim 6$ atoms. Plugging all these parameters into the initial equation gives our coupling efficiency η_{fiber} around 1$\sim$2%.

This experiment shows that TNF can be used as an effective tool to detect the existence of a few atoms through probing their fluorescence. Literatures also show that the Purcell effect could also happen in the vicinity of a TNF due to the modification of the vacuum modes in the presence of the strongly guided fundamental mode.

3.4 Analysis of MOT temperature and calculation of dipole trap

MOT temperature analysis Assuming that the cooling and trapping forces from all dimensions are approximately the same, the temperature of the MOT cloud is determined from the average speed of the trapped atoms, i.e., $k_B T/2 = m < v^2 > /2$. Combining Eq. (3.7), the temperature of the MOT atoms in steady state is given by Eq. (3.8).

$$< v_i >^2 = \frac{\hbar}{2m} \frac{\Delta^2 + (\Gamma/2)^2 + \Omega^2/2}{|\Delta|} \tag{3.7}$$

$$T = \frac{\hbar}{2k_B} \frac{\Delta^2 + (\Gamma/2)^2 + \Omega^2/2}{|\Delta|} \tag{3.8}$$

Given our experimental parameters: cooling laser $\lambda = 780.233$nm, red detuned by around 20MHz; TNF diameter around 450nm; beam diameter around 2.5cm; dipole moment of the $5S_{1/2} \rightarrow 5P_{3/2}$ transition $3.58424 \cdot 10^{-29}$ C·m, we can calculate the field magnitude then the Rabi frequency through $\Omega =$ dipole moment $\times$ field magnitude$/\hbar =$ dipole moment $\times \sqrt{\frac{\text{cooling laser power}}{c \times \varepsilon_0 \times \pi \times \text{beam area}}}/\hbar$. Fig. 3.13 shows the variation of MOT temperature as changing cooling laser power and detuning, respectively. Starting from the Doppler cooling limit, the temperature of the atoms in the MOT increases linearly with increasing the cooling laser power; For a total power of 7.2mW, the minimum temperature 199.5μK happens at a red detuning of 26.1MHz. When the detuning is very small, the on-resonance laser makes the scattering rate very large, which in turn heats up the atoms significantly. When the detuning is too large, the laser is too far away from resonance and no enough atomic scattering happens to cool down the atoms.

Dipole trap calculation Without trapping atoms through the TNF, as shown in the previous section, the average interacting atomic number and the coupling efficiency are very low. Thus our near-future plan is to set up a two-color dipole trap through the TNF, which has already been investigated a lot in the literature[17]. Here I give calculation for a two-color dipole trap based on the parameters of our own fabricated TNF.

The calculation I did in this thesis is for using circularly polarized light beams at the input.

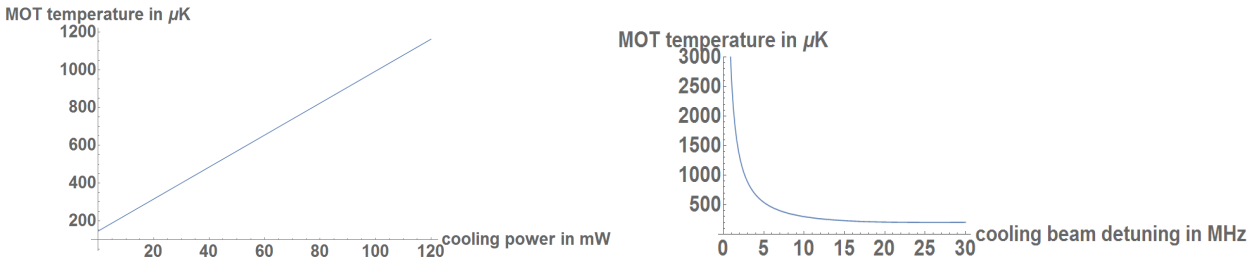

Figure 3.13: (left) MOT temperature in μK as a function of cooling laser power in mW, starting from Doppler cooling limit $\sim 145\mu$K with detuning 20MHz; (right) MOT temperature in μK as a function of cooling laser $|$detuning$|$ at a total power of 7.2mW

In this case, a set of trapping minima of the potential in the transverse plane is formed as a ring around the fiber waist. Using linearly polarized light beams to form dipole trap can be calculated in a similar way. The only difference is that the potential has two local minimum points in the transverse plane and the atoms are confined along those two straight lines parallel to the fiber axis. To calculate the latter case, Eq. (2.7) should be used to get the time-averaged intensity of the electric field while for circular polarization, I am using Eq. (3.9) for mode i outside the fiber, in which g_{out}, w_i and f_i are calculated in the same way as in Eq. (2.7) and noticeably, we do not have those terms depending on ϕ. Here I name the blue-detuned field *mode 1* and the red-detuned field *mode 2* and calculate their mode intensities respectively through Eq. (3.9)[17] then get their repulsive and attractive potentials by substituting into Eq. (3.10)[2].

$$|E_i|^2_{\text{out}} = g^2_{\text{out}}[K_0^2(q_i r) + w_i K_1^2(q_i r) + f_i K_2^2(q_i r)] \tag{3.9}$$

$$U_i = -\frac{1}{4}\alpha_i |E_i|^2 \tag{3.10}$$

$$\alpha(\omega) = \frac{e^2}{m_e}\sum_j \frac{f_{aj}(\omega_{ja}^2 - \omega^2)}{[(\omega_{ja}^2 - \omega^2)^2 + \gamma_{ja}^2\omega^2]} \tag{3.11}$$

Here $\alpha_i = \alpha(\omega_i)$ is the real part of the atomic polarizability at the optical frequency ω_i. The subscript i represents the number of fields we are going to calculate: i=1 and 2. The fact that the atomic dipole is induced by the field contributes one 1/2 and the averaging of the field intensity

over optical oscillations contributes to the other 1/2, which results in the 1/4. The function $\alpha(\omega)$ for a ground-state atom is given by Eq. (3.11)[17], in which e and m_e are the electric charge and mass of the electron and ω_{ja}, f_{aj} and γ_{ja} are the frequency, absorption oscillator strength and damping rate, respectively, of the spectral line ja.

Since the atomic motion, which has a timing scale of MHz, is much slower than the beating period of the two-color light fields, which has a timing scale of THz, the total potential is simply $U = U_1 + U_2$. The sign of the optical potential of each mode is determined by the sign of the field detuning: $\Delta_1 > 0$ ($\omega_1 > \omega_{ja}$), results in $\alpha_1 < 0$ so that repulsive potential $U_1 > 0$ while $\Delta_2 < 0$ ($\omega_2 > \omega_{ja}$), results in $\alpha_2 > 0$ so that attractive potential $U_2 < 0$. Since the blue-detuned light has a shorter wavelength, when its intensity is high enough, the net potential U is repulsive at short range and attractive at long range away from the fiber surface, which possesses a local minimum point, where the two forces cancel each other (The slope of the potential is zero.), leading to the possibility of atom trapping. Table 3.3 lists all the parameters used to calculate the dipole potentials for ^{87}Rb atoms trapping based on our fabricated TNF.

The ground-state Rb atom has two strong transitions, at 780nm (D_2 line) and 795nm (D_1 line). The calculation in this section for trapping the atom uses blue- and red-detuned lights with wavelengths $\lambda_1 = 651$nm and $\lambda_2 = 951$nm, respectively. The detunings of the laser beams from the dominant D_2 line of the atom are $\Delta_1/2\pi = 76$THz and $\Delta_2/2\pi = -69$THz. The fiber radius is at its optimal value 179 nm. Based on these values, Eq. (2.1) is first used to calculate the propagation constants for these two fields: $\beta_1 = 10.8 \times 10^6 \mathrm{m}^{-1}$ and $\beta_2 = 6.75 \times 10^6 \mathrm{m}^{-1}$. Then Eq. (3.9) is used to obtain the field intensities, which are subsequently substituted into Eq. (3.10) to get the potentials. For the above parameters, I find $q_1 a \approx 0.882$ and $q_2 a \approx 0.248$ so the corresponding evanescent decay lengths are $\Lambda_1 = 1/q_1 \approx 203$nm and $\Lambda_2 = 1/q_2 \approx 724$nm. Thus obviously this fiber radius is small enough to create a large ratio of $\Lambda_2/\Lambda_1 \approx 3.6$ so that atoms are possible to be trapped close enough to the fiber without falling onto it in a deep potential well.

Due to the circular polarization of the input fields, $U = U_1 + U_2$ is cylindrically symmetric.

Parameters	**Symbol**	**Values**
Speed of Light	c	$2.997\,924\,58\times10^{8}$ m/s
Permittivity of Vacuum	ε_0	$8.854\,187\,817\times10^{-12}$F/m
Boltzmann's Constant	k_B	$1.380\,648\,52\times10^{-23}$ $m^2kgs^{-2}K^{-1}$
Magnetic Permeability	μ_0	$4\pi\times10^{-7}$ H·m^{-1}
Elementary Charge	e	$1.602\,176\,565\times10^{-19}$ C
Electron Mass	m_e	$9.109\,382\,91\times10^{-31}$ kg
Refractive index of the silica fiber after pulling	n_1	1.45
Refractive index of air	n_2	1.0
Radius of the TNF waist	a	780.246nm×0.23
Rb87 D2 transition frequency	$\omega_{5^2S_{1/2}\to5^2P_{3/2}}$	2π·384.230 484 468 5(62) THz
Rb87 D1 transition frequency	$\omega_{5^2S_{1/2}\to5^2P_{1/2}}$	2π·377.107 463 380 (11) THz
Rb87 D2 line absorption oscillator strength	$f_{5^2S_{1/2}\to5^2P_{3/2}}$	0.695 77(29)
Rb87 D1 line absorption oscillator strength	$f_{5^2S_{1/2}\to5^2P_{1/2}}$	0.342 31(97)
Rb87 D2 line Decay Rate/Natural Line Width	$\gamma_{5^2S_{1/2}\to5^2P_{3/2}}$	$38.117(11)\times10^{6}$s^{-1}
Rb87 D1 line Decay Rate/Natural Line Width	$\gamma_{5^2S_{1/2}\to5^2P_{1/2}}$	$36.129(35)\times10^{6}$s^{-1}

Table 3.3: Parameters used in this section to calculate atomic dipole trap potentials

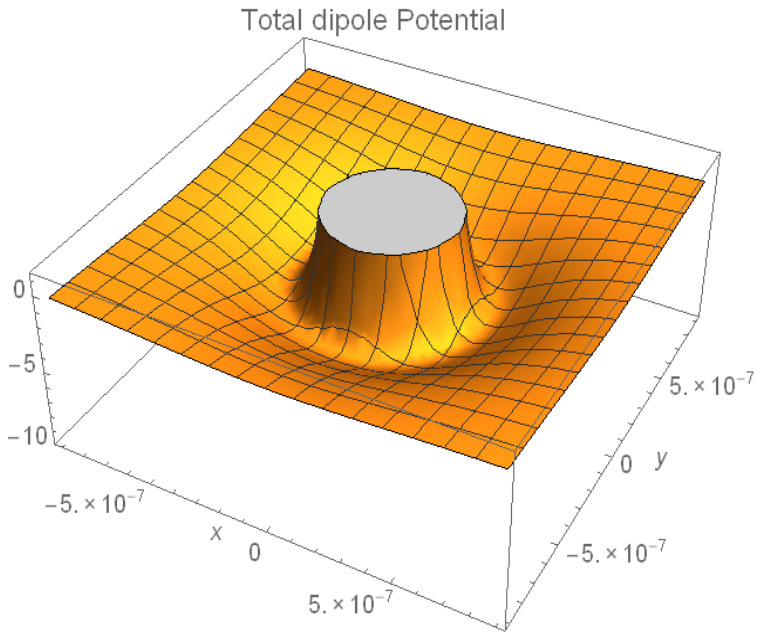

Figure 3.14: Transverse-plane profile of the total two-color dipole potential U from circularly polarized beams at the input with parameters given in the context

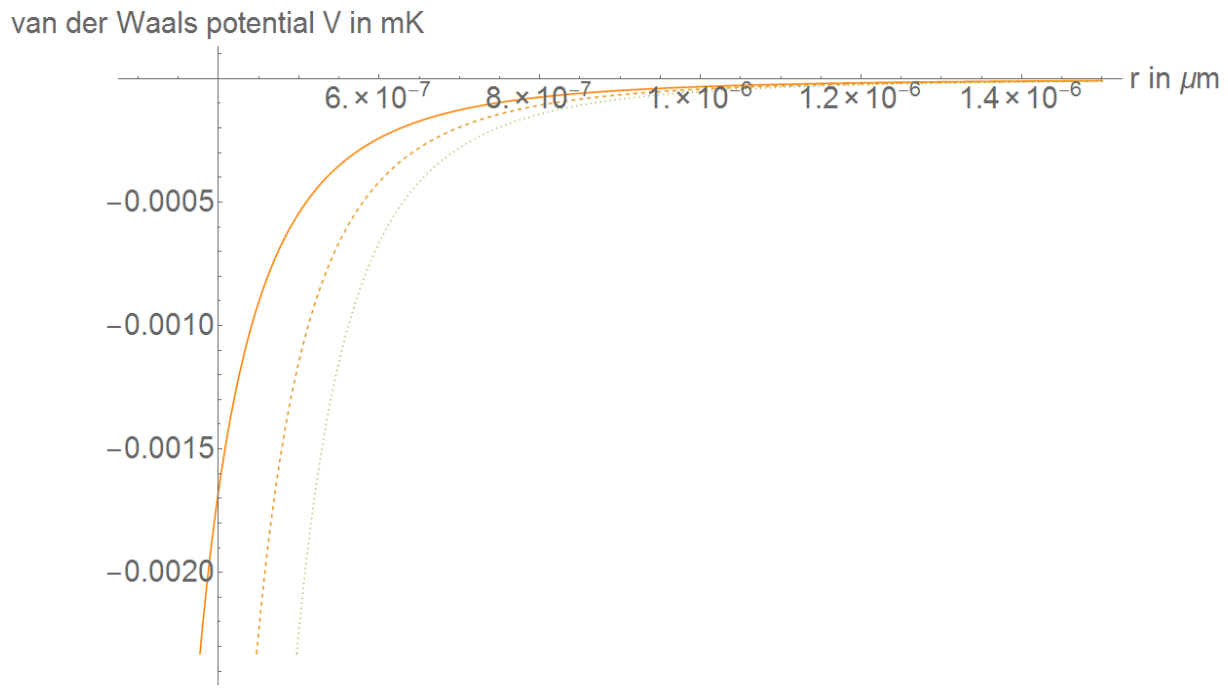

Figure 3.15: van der Waals potential V of a ground-state Rb atom near a TNF for different fiber radiuses

In Fig. 3.14, I plot the spatial profile of U in the fiber transverse plane. The figure shows that the potential is independent of the azimuthal angle ϕ and has a set of deep minima formed as a ring surrounding the fiber. The atoms can still move freely along the fiber axis so U is also z-independent, as a result, the full potential is a cylindrical shell at the minima in the 3D space.

An atom near the surface of a medium experiences a van der Waals potential as well. We routinely produce TNF with diameter between 400 and 500nm in our lab, which is usually larger than the atom-to-surface distance $D = r - a$, so in this thesis, I calculate the van der Waals potential according to flat-surface bulk-medium van der Waals potential formula $V = -C_3/D^3$. Here the coefficient C_3 is equal to $4.94 \times 10^{-49}\mathrm{Jm}^{-3}$ and $7.05 \times 10^{-49}\mathrm{Jm}^{-3}$ for the $5S_{1/2}$ and $5P_{3/2}$ levels, respectively of ^{87}Rb near fused silica[18]. In Fig. 3.15, I plot the van der Waals potential V of a ground-state Rb atom near a silica fiber as a function of D for different fiber radii. The results show that a smaller fiber radius leads to a smaller absolute potential magnitude and a less steep slope of the potential.

The total potential U_{tot} of the atom is the sum of the optical dipole potential U and the van

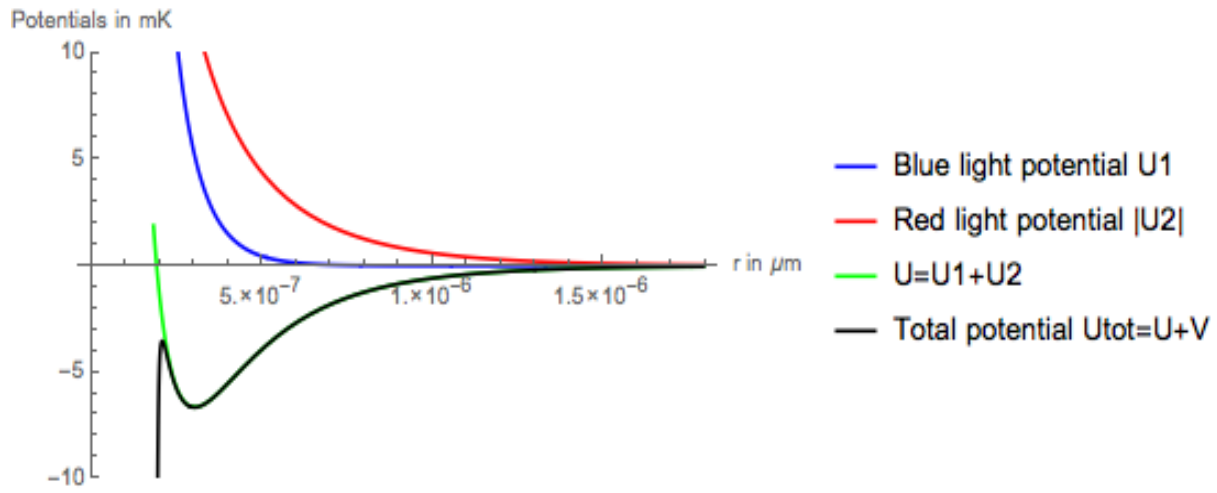

Figure 3.16: Total potential of a ground-state Rb atom outside a vacuum-clad subwavelength silica fiber including all the contributions: dipole optical potentials with $P_1 = 10\text{mW}$ and $P_2 = 15\text{mW}$ and van der Waals potential

der Waals potential V, i.e., $U_{\text{tot}} = U + V$. In Fig. 3.16, I plot the total potential (black) as well as all the contributions: blue-detuned repulsive potential (blue), red-detuned attractive potential (red) and their sum (green). The figure shows that the evanescent decay length of the red-detuned light is significantly larger than that of the blue-detuned light. The net optical potential U has a local minimum value $U_m \approx -7\text{mK}$ at $r_m \approx 300\text{nm}$, well outside the fiber. The van der Waals potential is only about $-1.5\mu\text{K}$ at the local minimum point thus just makes a small contribution in the vicinity of the trapping minimum. However, van der Waals potential does make the height of the wall of the total potential close to the fiber surface drop significantly.

Finally, Fig. 3.17 illustrates the effects of changing the powers of blue- (P_1) and red-detuned (P_2) light on the total potential. As seen from the left figure, an increase in P_1 leads to a decrease in the depth of the trapping potential as well as a shift of the local minimum point r_m farther away from the fiber surface. Also, the height of the repulsive wall in the region of $r < r_m$ is increased. As seen from the right figure, an increase in P_2 leads to an increase in the depth of the trapping potential as well as a shift of the local minimum point r_m towards the fiber surface. Also, the height of the repulsive in the region of $r < r_m$ is reduced. The comparison between the left and right figures shows that P_1 and P_2 have opposite effects on the total potential. Thus to produce

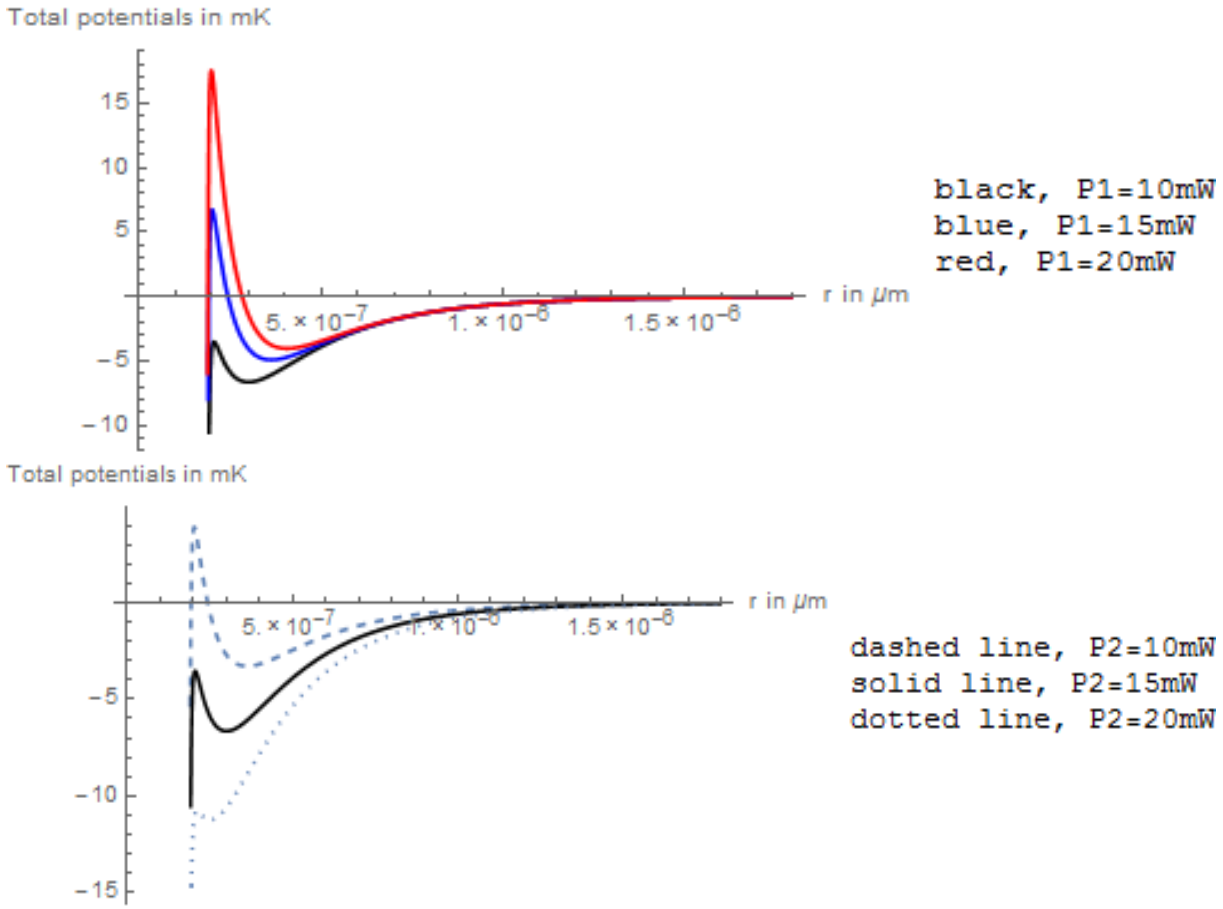

Figure 3.17: (top) Effect of the power P_1 on the total potential U_{tot} with $P_2 = 15\text{mW}$; (bottom) Effect of the power P_2 on the total potential U_{tot} with $P_1 = 10\text{mW}$.

a potential with a deep trapping minimum outside the fiber and with a high repulsive wall in the region of $r < r_m$, the ratio between P_1 and P_2 must be optimized appropriately[17].

Comparing to Fig. 3.13, we can see that the potential calculated as an example in this section ($\sim$ several mK) is enough to trap atoms in a normal MOT cloud ($\sim$ several hundreds of μK). The parameters used here are adjustable and the calculation can be repeated when the actual experiment is implemented. Proper parameters should be chosen based on the actual experimental conditions.

Chapter 4

Conclusion and Outlook

In my thesis, I have presented in detail our efforts in building up a MOT-TNF interface experimental platform from the very beginning. I was myself involved in both of the two parts: fabricating the TNF and making improvements on fiber pulling as well as setting up the MOT in the UHV system. Up to now, this project has made certain progress and we are investigating how to enhance the light-matter interaction in our experiments.

The investigations we have done to this system are as follows: We performed thermal dynamics characterization on our TNF through an interferometric measurement of the nanofiber temperature. We characterized some of our MOT parameters, for example, its approximate lifetime, the number of atoms trapped, the size and density of the atomic cloud through a free-space absorption experiment as well as its temperature. We also performed an experiment of using the TNF as a tool to probe a single atom around the nanofiber waist. The effective number of atoms around the TNF in our setup is $3 \sim 6$ and the spontaneously emitted photons that coupled into the fundamental mode being guided through the fiber have been effectively detected in our experiment. This shows a coupling efficiency between $1 \sim 2\%$ for our MOT-TNF interface.

Some challenges and our efforts on improving them are also described in my thesis. First, a clean enough fiber with a high transmission will be the next goal to achieve. We are making modifications to our fiber pulling rig, for example, improving the torch and the pulling algorithm, adding oxygen into the gas line, getting a more accurate flow rate metrology, adding a flow box to make the pulling environment cleaner and so on. Once we are able to launch several mW laser into our TNF, we can move forward to set up the dipole trap, which has been implemented as a popular and matured technology in other groups ([19] and [20] for instance) to highly increase the number of trapped and interacted atoms.

The purpose of forming a dipole trap is to significantly increase the optical depth through trapping more atoms close to the fiber surface. For example, Rauschenbeutal's group achieved an O.D. of 32 in 2010 and Kimble's group achieved an O.D. of 66 in 2012. In a standard optical dipole trap, a far red-detuned laser field will be sent through the nanofiber with a certain polarization creating a dipole attractive potential, which reaches its maximum at the fiber boundary, as we showed in Section 2.2. This 1D standing wave formed by the red laser will prevent the atoms from drifting away the fiber surface. Also a far blue-detuned laser will also be launched through one end of the fiber to generate a dipole repulsive force that helps avoid the atoms falling onto the fiber surface due to the Vander Waals attraction. Since the blue-detuned laser has a much shorter decay length, the combination of these two dipole forces will form an optical lattice that traps the atoms around 100$\sim$200nm away from the fiber surface. The power of the laser beams determines the temperature of the atoms the trap will be able to hold, with higher power corresponding to a deeper trap, able to hold hotter atoms. In this thesis, I calculated in detail this two-color dipole trap mechanism using circularly polarized light in section 3.4 and compared the results to our MOT temperature.

This is the main motivation behind all our efforts in getting a high quality nanofiber that can stand enough laser power for setting up the dipole trap. Once we achieve this goal, we will be able to pursue some interesting experiments and investigations further, as described in Chapter 1, such as the development of an optical quantum memory based on EIT mechanism; exploration of optical non-linearity at single photon, single atom level; cross phase modulation; creation of fiber-coupled-single-photon source based on DLCZ protocol and investigation on coupling between trapped atoms with cavity QED or a opto-mechanical resonator and so on.

Bibliography

[1] H. Schmidt and A. Imamoglu. *Giant kerr nonlinearities obtained by electromagnetically induced transparency.* Optics letters, 21(23): 1936–1938, 1996.

[2] John D. Jackson. *Classical Electrodynamics.* John Wiley and Sons, 1999.

[3] G. Sague Gassany. *Cold atom physics using ultra-thin optical fibres.* PhD thesis, Vienna University of Technology, Institute of Atomic and Subatomic Physics, 2008.

[4] Fam L. Kien, K. Hakuta et al. *Field intensity distribution and polarization orientations in a vacuum-clad subwavelength-diameter optical fiber.* Optics Communications, 242: 445-455, 2004.

[5] Timothy A. Birks and Youwei W. Li. *The shape of fiber tapers.* Journal of Lighwave Technology, 10(4): 432-438, April 1992.

[6] Aveek Chandra. *Tapered optical nanofiber for light-atom interfacing.* Master thesis, University of Calgary, 2014.

[7] Jonathan Hoffman. *Optical nanofiber fabrication and analysis towards coupling atoms to superconducting qubits.* PhD thesis, The University of Maryland, 2014.

[8] Matthew Borselli. *High-Q Microresonators as Lasing Elements for Silicon Photonics.* PhD thesis, California Institute of Technology, 2006.

[9] K. Toubaru M. Fujiwara and S. Takeuchi. *Optical transmittance degradation in tapered fibers.* Opt. Express, 19(8596), 2011.

[10] James D. Franson Meimei Lai and Todd B. Pittman. *Transmission degradation and preservation for tapered optical fibers in rubidium vapor.* Applied Optics, 52(12), 2013.

[11] C. Wuttke and A. Rauschenbeutel. *Thermalization via heat radiation of an individual object thinner than the thermal wavelength.* Phy. Rev. Lett, 111(024301), July 2013.

[12] Christopher J. Foot. *Atomic Physics.* Oxford University Press, 2005.

[13] Harold J. Metcalf and Peter Straten. *Laser Cooling and Trapping.* Springer Press, 1999.

[14] Daniel Adam Steck. *Rubidium 87 D Line Data.* page 25, December 2010.

[15] Lucia Duca. *Implementation and testing of a magneto-optical trap for neutral ^{87}rb atoms for quantum information processing.* Universita' di Bologna, 2009.

[16] M. Morinaga F. Kien V. Balykin K. Nayak, P. Melentiev and K. Hakuta. *Optical nanofiber as an efficient tool for manipulating and probing atomic fluorescence.* Optics Express, (15): 5431-5439, 2007.

[17] V. I. Balykin Fam Le Kien and K. Hakuta. *Atom trap and waveguide using a two-color evanescent light field around a subwavelength-diameter optical fiber.* Physical Review A, 70(063403), 2004.

[18] L. A. Orozco, S. L. Rolston et al. *Photon-correlation measurements of atomic-cloud temperature using an optical nanofiber.* Physical Review A, 92(013850), 2015.

[19] Eugen Vetsch. *Optical interface based on a nanofiber atom-trap.* PhD thesis, Johannes Gutenberg-Universitat in Mainz, 2010.

[20] D. Alton, H.J. Kimble et al. *Demonstration of a state-insensitive, compensated nanofiber trap.* Phy. Rev. Lett, 109(033603), 2012.

[21] Miguel Juarez. *The use of a lock-in amplifier to stabilize the frequency of a diode laser.* College of the Holy Cross, 2009.

[22] Pavel Zhuravlev. *Development of a stable laser lock system.* University of William and Mary, 2012

[23] The program is available at the Digital Repository of the University of Maryland (DRUM) at http://hdl.handle.net/1903/15069.

Appendix A

Procedure for fiber pulling and fiber feedthrough

Fiber pulling procedure

The fiber pulling is performed in Professor Paul Barclay's nanophotonics lab so communication with the students working there before scheduling our pulling would be necessary.

1. Turn-on list

    - Computer that controls the motors and the microscope
    - Motor Controllers (two of them)
    - Light source for microscope
    - Photodetector (the nanosecond visible light detector)
    - UV-glue curing controller (at least 5 minutes before using)
    - Velocity diode laser (fiber coupled, wavelength 635-640nm)
    - Check fiber connection: check from the mating sleeve whether the visible laser is coupled into fiber cable F, which should be spliced to our fiber scroll. If necessary, splice it to our fiber scroll.

2. Preparing the fiber for pulling

    - Remove the jacket at one end of the bare fiber
    - Cleave this end, clean it using Isopropyl alcohol (IPA)
    - Connect it to the Photodetector
    - See the transmission on screen, adjust the laser power if necessary
    - Strip fiber for pulling (give long enough arm) and clean it using IPA
    - Align it in clamps (initialize if necessary)
    - Check parameters on computer before pulling (refer to Tables 2.3 and 2.4)
    - Bring the fiber microscope to focus on the fiber core and see it on screen
    - Open the valves for gases, check the gas level (refer to Tables 2.3 and 2.4), adjust the flow meters if necessary, light the torch

3. Pulling

- Put the panel, engage the flame and start pulling
- ‘‘Delete and Reset’’ the data collection before the power dropping and keep monitoring the transmission
- Disengage the flame and stop pulling when the transmission spectrum is back to single-mode, adjust the microscope to see the fiber waist
- Close the gas valves
- Adjust tension if necessary to make the tapered part straight, monitor the fiber transmission simultaneously
- Estimate the transmission and save the data file

4. Fiber extraction

- Prepare the fiber extraction device, connect the C-shape bracket, chemical clamp and translational stages
- Find the best position for the bracket under the fiber and align the fiber in the grooves
- Drop glue on both ends of the bracket and cure the glue for about 3s (remove any residual glue from the grooves using heating gun first) until it becomes solid, monitor the transmission at the same time
- Remove the fiber for the feed-through, disconnect it from the photodetector and cut it from the other end (give long enough arm)

5. Turn-off list

- UV-glue curing controller
- Motor Controllers (two of them)
- Light source for microscope
- Photodetector
- Velocity diode laser

Fiber feedthrough procedure

After successfully getting a tapered nanofiber, it has to be protected intact and transferred to our lab for launching into the UHV chamber.

- Connect one end of the C-shape bracket to the feed-through arm, carefully tighten the two screws on each side then disconnect the bracket from the chemical clamp
- Clean the fiber arms using IPA and feed the arms through the hole in the top flange
- Clean the teflon, feed both ends of the fiber through the teflon
- Clean the nut, feel both ends of the fiber through the nut
- Tighten the nut using a wrench (This is a **crucial** step and tightening by hands is **NOT** enough.)
- Put the six screws back in the flange and install the acrylic cylinder
- Transfer the fiber
- Check the transmission of the patch cable, optimize it if necessary
- Cleave the ends of the fiber arms and splice them with the patch cable ends, check the transmission again after splicings and record the losses
- Put a new gasket on top of the chamber and carefully feed through the fiber
- Adjust the position of the fiber by rotating the flange to enable the best position of the bracket for not blocking the MOT beams
- Close the MDC valve, tighten the six screws and start the mechanical pump
- Keep monitoring the TNF transmission from the power meter and the pressure from the multimeter
- Start the Turbo pump as the pressure reaches around 10^{-3} torr
- Open the MDC valve slowly and monitor the TNF transmission
- If no leakage, turn on the Ion pump as the pressure reaches 10^{-5} torr
- Wait for a good enough vacuum while monitor the TNF transmission

Appendix B

Our home-made laser lock-in amplifiers

There are many references on this well-established laser-locking technique. The first version of our home-made Lock-in Amplifier is based on [21] and [22], in which the basic principle of how it works is very well described (also [6]) and electronic schematics are also provided. The second version has some improvement, contributed by Kenzo Makino from University of Tokyo as he was working in our group as a visiting student. Both of these two versions are included in Fig. B.1 and Fig. B.2 and the explanation can be found in [22]. Some values of electronic components need to be adjusted according to our specific experimental parameters.

Here a simple procedure of how to tune it to work with our home-made ECDLs is included but experience should accumulate with times of operation.

- First test the Lock-in amplifier itself by giving the dither and spectroscopy inputs the same in-phase sinusoidal signal, as shown in Fig. B.3 (above).
- Tuning the phase of the dither signal until these two channels are in phase to the mixer, then the mixer output signal should be like Fig. B.3 (below).
- Check the SNR of the saturated absorption peak from the oscilloscope: usually by experience 100-200mV is enough for the Lock-in to work effectively.
- Feed dither signal to the piezo in ECDL and check whether the absorption peak is dithered normally as well as the monitor signal (The correct monitor signal is the scanned spectroscopy signal times a TTL signal.).
- Slowly reduce laser scanning on resonance and check the monitor signal (The correct one is $\cos(2\omega_d t)$ times a TTL signal of frequency ω_d, in which ω_d is the dither signal frequency.).
- If everything up to this step is correct, look on oscilloscope at the error signal, which should be a moving DC signal from negative to positive offset when the loop is ON.

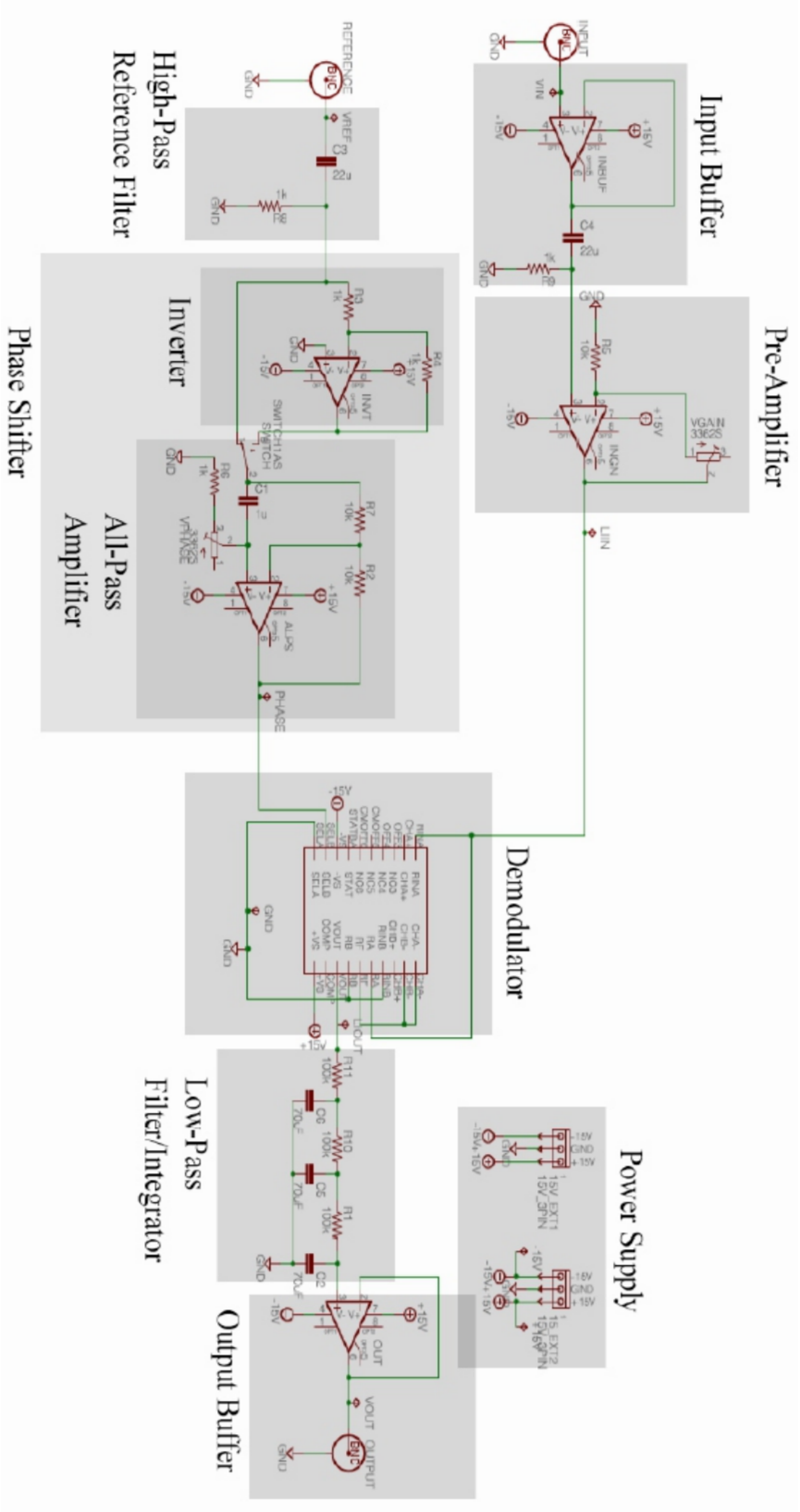

Figure B.1: The first version of our home-made Lock-in Amplifier schematic (copy from Fig. 7 in [22])

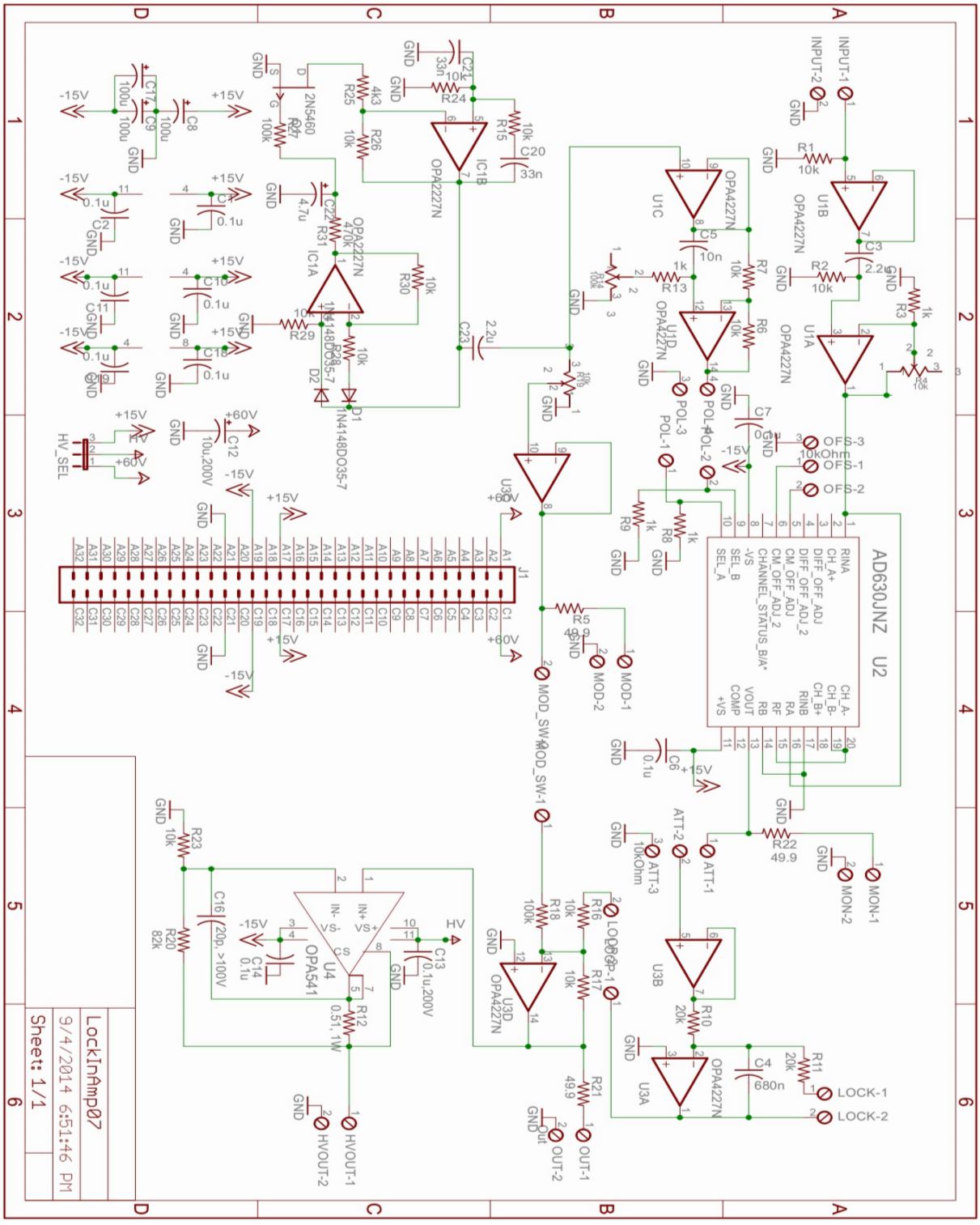

Figure B.2: The second version of our home-made Lock-in Amplifier schematic (contributed by Kenzo Makino as a visiting student from University of Tokyo)

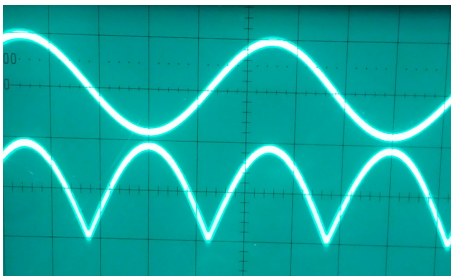

Figure B.3: (above) the signal given to dither and spectroscopy inputs; (below) the output signal of mixer as a monitor signal

- Turn on “Integral” (i.e., the low pass filter at the end of the Lock-in schematic) and observe the error signal (The correct one should be a moving-up DC signal if the phase is positive and a moving-down DC signal if the phase is negative.).
- The final step also the best way is to test the locking efficiency with MOT ON. If everything seems correct up to this step but turning on the “loop” followed by the “integral” makes the MOT dimmer/less bright, it could be either that the dither signal is too strong for the ECDL or the total gain is too high. Try to reduce the amplitude of the dither signal to the piezo (can increase the gain from the pre-amplifier on the spectroscopy signal at the same time) or reduce the total gain.
- If turning on the “loop” followed by the “integral” makes the MOT disappear, check the phase matching between the two input channels.
- If it seems that the Lock-in works by itself but does not work on the ECDL, try to increase the amplitude of the dither signal and the pre-gain on the spectroscopy signal and observe. Maybe increasing the total gain is also helpful.
- Finally, check the Lock-in performance by timing its locking duration. Usually, if the ECDL is relatively stable, locking the laser on resonance and having the MOT for half an hour is not a big problem.
- To unlock the laser, first turn off the “integral” then the “loop” and turn off the dither signal.